Physics of Fluids

RESEARCH ARTICLE | MARCH 04 2025

Frequency response analysis of jet–vortex interaction for variable relative spacing

M. Garrido-Martin ; Francisco J. Blanco-Rodríguez ; P. Gutierrez-Castillo ; Tobias Bölle ; C. del Pino

Check for updates

Physics of Fluids 37, 034103 (2025)
https://doi.org/10.1063/5.0253818

View Online Export Citation

Articles You May Be Interested In

Optimal response of Batchelor vortex

Physics of Fluids (June 2017)

Modal and non-modal evolution of perturbations for parallel round jets

Physics of Fluids (April 2015)

Transient growth of secondary instabilities in parallel wakes: Anti lift-up mechanism and hyperbolic instability

Physics of Fluids (November 2011)

07 March 2025 08:03:06

AIP Publishing

Physics of Fluids

Special Topics Open for Submissions

Learn More

AIP Publishing

Physics of Fluids ARTICLE pubs.aip.org/aip/pof

Frequency response analysis of jet–vortex interaction for variable relative spacing

Cite as: Phys. Fluids **37**, 034103 (2025); doi: 10.1063/5.0253818
Submitted: 19 December 2024 · Accepted: 23 January 2025 ·
Published Online: 4 March 2025

View Online Export Citation CrossMark

M. Garrido-Martin,[1,a)] Francisco J. Blanco-Rodríguez,[2] P. Gutierrez-Castillo,[1] Tobias Bölle,[3] and C. del Pino[1]

AFFILIATIONS

[1]Universidad de Málaga, Institute for Mechatronics Engineering and Cyber-Physical Systems (IMECH.UMA), Campus de Teatinos, s/n 29071, Málaga, Spain
[2]Área de Mecánica de fluidos, Departamento de Ingeniería aeroespacial y Mecánica de fluidos, Camino de los descubrimientos, s/n 41092, Sevilla, Spain
[3]Deutsches Zentrum für Luft- und Raumfahrt, Institut für Physik der Atmosphäre, Oberpfaffenhofen, Germany

[a)]Author to whom correspondence should be addressed: manolouma@uma.es

ABSTRACT

This work presents frequency response analysis of the Lamb–Oseen vortex with a single-point injection (SPI) acting in the axial direction. In particular, we address the vortex response-mode selection as the radial location, a_f, of the SPI is varied. We interpret these results by complementary linear stability and resolvent analyses. Our results demonstrate a way to excite certain modal behavior of the optimal response using SPI. Energy gain maps of the frequency response as a function of the streamwise wavenumber and the location and frequency of the SPI show that the modes with azimuthal wavenumbers $|m| = 0$ and $|m| = 1$ have the highest gain and correspond to different known families of Kelvin vortex waves. The value of a_f strongly influences the occurrence and importance of the dominant vortex response modes. In particular, for relatively low a_f values, the axisymmetric mode dominates. However, as a_f is increased, the dominant modes shift to helical modes. Additionally, we identify non-normal effects in specific areas of the parameter space, highlighting two particular regions: (i) an area explained only by the viscous critical layer characterized by a concentrated ring and (ii) a region given by the resolvent analysis for short-wavelength perturbations that exhibits a combination of the ring and a distinctive helical mode near the vortex core. Finally, we prove that flow patterns obtained at the maximum gain points of the frequency response exhibit a similar behavior to the optimal response, thus confirming the SPI as a powerful candidate to promote the optimal response in practical applications.

© 2025 Author(s). All article content, except where otherwise noted, is licensed under a Creative Commons Attribution (CC BY) license (https://creativecommons.org/licenses/by/4.0/). https://doi.org/10.1063/5.0253818

07 March 2025 08:03:06

I. INTRODUCTION

The kinematics and dynamics associated with jet–vortex interactions are of considerable interest for various applications in aeronautics. In particular, the interaction between a line vortex and a collinearly aligned jet flow constitutes a prototypical configuration of the near airplane wake. Due to their long persistence, trailing vortices govern wake evolution and are, thus, of interest in various respects, e.g., for the formation of contrails and the hazard of aircraft encounter (Spalart, 1998; del Pino *et al.*, 2011; Paoli and Shariff, 2016; García-Ortiz *et al.*, 2019; and Smith and Ventikos, 2021). The main hazard is procured by the strong rotation associated with trailing vortices and is operationally accounted for by introducing conservative waiting times between aircraft on landing and takeoff operations as described by Spalart (1998) and Jacquin *et al.* (2003). Hence, considerable interest in rapidly alleviating trailing vortices and different control strategies to reduce the vortex strength have been proposed (Holzäpfel *et al.*, 2002; Dghim, Ferchichi, and Fellouah, 2020; García-Ortiz *et al.*, 2020; Qiu *et al.*, 2021; and Gharbia *et al.*, 2024). A prototypical control strategy for trailing-vortex alleviation assumes a pulsed jet injection installed close to the wingtip undertaken experimentally by Zaccara *et al.* (2022, 2023, 2024).

Experimental trailing vortices at realistic Reynolds numbers are typically well approximated by the Moore–Saffman vortex or two-scale models as presented by Moore and Saffman (1973) and Jacquin *et al.* (2001), respectively. Also Batchelor (1964) captures essential characteristics of experimentally realized trailing vortices with axial velocity component as shown by del Pino *et al.* (2011) and Bölle *et al.* (2023). The axial velocity component of these models induces a

© Author(s) 2025

parameter range of asymptotically unstable modes, see, e.g., Fabre and Jacquin (2004) and Feys and Maslowe (2014), while the limiting case of vanishing axial velocity, called Lamb–Oseen vortex, is asymptotically stable as first reported by Lessen *et al.* (1974) and later confirmed by Mayer and Powell (1992). However, the parameter range of asymptotic instability seems not usually realized in experiments, where trailing vortices are systematically found to be stable (Edstrand *et al.*, 2016; Bölle *et al.*, 2023; and Bölle, 2023). Due to the non-normality of the linearized Navier–Stokes operator for the above-mentioned vortex models, considerable transient growth is possible (Antkowiak and Brancher, 2004, 2007; Pradeep and Hussain, 2006; and Heaton and Peake, 2007). However, unlike linear stability, Heaton and Peake (2007) and Bölle *et al.* (2021) reported that these non-normal dynamics seem to be universal and apply to all above-mentioned vortex models. This finding was corroborated by Fontane *et al.* (2008) with stochastic-forcing and by many others (Viola *et al.*, 2016; Guo and Sun, 2011; and Bölle *et al.*, 2021) using resolvent analysis (Rolandi *et al.*, 2024). The operational mechanisms identified in these studies are particularly relevant for jet–vortex interactions if the injection is located in the periphery of the vortex. In fact, Bölle *et al.* (2021) showed that the receptivity of the vortex to perturbations localized in the free-stream is necessarily associated with the non-normal dynamics. We, therefore, restrict our analysis to the Lamb–Oseen vortex. Physically, this receptivity can be understood by the mother–daughter mechanism originally proposed by Boberg and Brosa (1988) for pipe flow and adapted by Bölle (2021) for the receptivity of vortex flows.

Recently, Zaccara *et al.* (2023) addressed the same control problem, however, concentrating on the excitation of Crow (Crow, 1970) and Widnall (Widnall *et al.*, 1974) instabilities in the counter-rotating vortex pair. Here, we assess the excitation mechanism on a generic level, considering various frequency bands and discuss the different excitation mechanisms. While the dynamics of an isolated vortex has been studied in considerable detail, it is not immediately evident how these perturbations can actually be excited and how robust control devices should be implemented in practice. This is in part because the spatial patterns of optimal perturbation or forcing are intricate and cannot be generated using practical control devices.

A frequency response (FR) analysis was performed by Blanco-Rodríguez *et al.* (2016) to assess the linear response dynamics of an isolated Lamb–Oseen vortex when subjected to sustained forcing by a coaxially aligned jet flow at a predefined radial distance and pulsating frequency. In their study, different spatial distributions of the injections were proposed, showing that by systematically varying the axial wavenumber and pulsation frequency several vortex Kelvin waves can be excited. In this work, we focus on a single punctual injection (SPI), as it yields the most pertinent vortex-response modes and because its implementation in practical control devices can be envisaged. However, the variation of the injection distance affects the mode selection along with the realizable amplification. As far as the authors know, this effect has not been addressed before. So, the main objective of this study is to understand the dynamics of an isolated vortex column as the forcing distance at which an axially oriented SPI is applied.

In order to interpret these results, we also conduct *linear stability* (LS) and *resolvent* analyses (RA) of the isolated vortex. These complementary studies help to identify the presence of non-normal effects excited by external forcing. Furthermore, we confirm the importance of placing the forcing in the critical layer of the vortex in certain non-normal regions for optimal amplification as shown by Le Dizès (2004) and Bölle *et al.* (2021). This also suggests that an optimal location for the application of an SPI exists.

The structure of the article is as follows. Section II briefly recalls the methodological techniques used in this study, i.e., linear stability, resolvent, and frequency response analyses for the Lamb–Oseen vortex. In Sec. III, we discuss an overview of the amplification characteristics as revealed by frequency response analysis. Section IV presents a detailed discussion of representative dynamic regimes and spatial structures of the perturbation response, and finally, Sec. V concludes the main findings.

II. LINEAR ANALYSIS OF VORTEX DYNAMICS

We consider the linear dynamics of an isolated line vortex evolving in an incompressible fluid at rest at infinity (see Fig. 1). In particular, we consider the parallel-flow approximation of the Lamb–Oseen vortex as a base flow which can be written (in the dimensional form) as

$$V(R) = \Omega(R)\,R = \Omega_c\,R_0\,\frac{1-\exp(-(R/R_0)^2)}{(R/R_0)}. \tag{1}$$

In the following, all quantities are non-dimensionalized using the rotation rate at the vortex center Ω_c and the radial coordinate R_0 at which the azimuthal velocity takes a value of $V = V_0(1-e^{-1})$, where $V_0 = \Omega_c\,R_0$, Ω_c, and R_0 being time and length scales, respectively. It must be noted that capital letters have been used throughout the manuscript to denote dimensional quantities. Hence, the velocity field $\bar{\boldsymbol{u}}$ of the Lamb–Oseen vortex in cylindrical coordinates (r,θ,z) reads

$$\bar{u}(r) = 0, \quad \bar{v}(r) = \frac{1}{r}\left(1-e^{-r^2}\right), \quad \bar{w}(r) = 0. \tag{2}$$

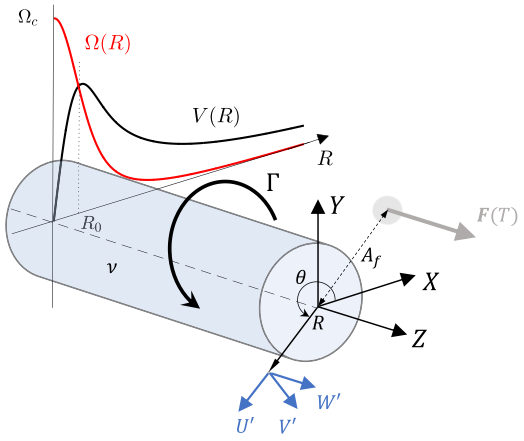

FIG. 1. Dimensional form of the problem setup: straight vortex tube of a fluid with a kinematic viscosity ν rotating at an angular velocity $\Omega(R)$ and the corresponding azimuthal velocity $V(R) = \Omega(R)\,R$, where the core radius is R_0 and Ω_c is the angular velocity at the centerline. The Cartesian coordinate system (X,Y,Z) is depicted in the plane where the problem is solved. The velocity perturbation field (U',V',W') in cylindrical coordinates (R,θ,Z) is also indicated. The contour (grayscale) of the harmonic $(\Omega_f = \Omega_c\,\omega_f)$ streamwise SPI volumetric forcing, $\boldsymbol{F}(T)$, located at a distance of $A_f = R_0\,a_f$ from the vortex center is also depicted.

07 March 2025 08:03:06

© Author(s) 2025

It is well-known that the above-mentioned model corresponds to a self-similar solution of the Navier–Stokes equations with a core size increasing linearly in time ($R_0(T)^2 - R_0(T=0)^2 \sim T$). However, the timescale of the viscous dissipation, which is $T_\nu = 2\pi R_0^2/\nu$, is two orders higher than the time horizon used in the simulations. Hence, the diffusion is ignored here, and the vortex is considered "frozen" with a constant radius, R_0 and, therefore, with a steady-state base flow.

With the normalization adopted, the Reynolds number is $Re = \frac{\Omega_c R_0^2}{\nu} = \frac{V_0 R_0}{\nu} = \frac{\Gamma}{2\pi\nu}$, where $\Gamma = \lim_{R\to\infty} 2\pi R V$ and ν are the vortex circulation and the kinematic viscosity of the fluid, respectively. Typical Reynolds numbers corresponding to vortex flows generated by aircraft correspond to $Re \approx 8000$, as performed experimentally by Edstrand *et al.* (2016). In particular, the Reynolds number considered for our base flow is $Re = 7940$.

The problem is governed by the (incompressible) Navier–Stokes equations which can be written as

$$\begin{aligned} \nabla \cdot \boldsymbol{u} &= 0, \\ \frac{\partial \boldsymbol{u}}{\partial t} &= -\boldsymbol{u}\cdot\nabla\boldsymbol{u} - \nabla p + \frac{1}{Re}\nabla^2\boldsymbol{u} + \boldsymbol{f}(\boldsymbol{x},\, t). \end{aligned} \tag{3}$$

However, the state of the system can be given by $\boldsymbol{z}(t) = (\boldsymbol{u}, p)(t)$, such that the velocity $\boldsymbol{u}$ is solenoidal, p is the pressure, and both fields satisfy the boundary conditions. While it is possible to work with this set of primitive variables directly [e.g., Bölle *et al.* (2021)], often a transformed set is used, for instance, to consider incompressibility directly (Antkowiak and Brancher, 2004; Fabre and Jacquin, 2004; and Blanco-Rodríguez *et al.*, 2016). Denoting this transformed state by $\boldsymbol{q}(t)$, we recover the primitive variables by the linear transformation $\boldsymbol{z}(t) = \boldsymbol{C}\boldsymbol{q}(t)$.

We assume the decomposition $\boldsymbol{q}(t) = \bar{\boldsymbol{q}} + \boldsymbol{q}'(t)$, where the base flow $\bar{\boldsymbol{q}}$ is taken as the steady-state, parallel-flow approximation of the Lamb–Oseen vortex and $\boldsymbol{q}'(t)$ denotes a small fluctuation.

Linearization of the incompressible Navier–Stokes equations (3) around the given base state and neglecting second-order perturbations then yields the (non-dimensional) linearized forced Navier–Stokes equation, which takes the generic form

$$\begin{aligned} \frac{\mathrm{d}\boldsymbol{q}'}{\mathrm{d}t} &= \boldsymbol{A}\boldsymbol{q}' + \boldsymbol{B}\boldsymbol{f}(\boldsymbol{x},\, t), \quad \boldsymbol{q}'(0) = \boldsymbol{q}_0, \\ \boldsymbol{z}' &\equiv (\boldsymbol{u}', p') = \boldsymbol{C}\boldsymbol{q}'. \end{aligned} \tag{4}$$

Here, $\boldsymbol{A}$ denotes the linearized Navier–Stokes operator evaluated at the base flow and $\boldsymbol{B}\boldsymbol{f}(\boldsymbol{x},\, t)$ constitutes an external forcing that results from either the synthetic effect of the neglected nonlinearities or external excitation applied to the flow. The explicit expressions of the entries of the matrices $\boldsymbol{A}$, $\boldsymbol{B}$, and $\boldsymbol{C}$ of the input–output system (4) can be found in Blanco-Rodríguez *et al.* (2017), which are a slightly modified version of those derived in Mao and Sherwin (2012).

Finally, the measure used to test whether a disturbance $\boldsymbol{u}'(t)$ is growing or decaying in time is its kinetic energy, $E(t)$, defined as

$$E(t) = \frac{1}{2}\langle \boldsymbol{u}', \boldsymbol{u}' \rangle, \tag{5}$$

where we assume $\boldsymbol{u}'(t)$ to pertain to an appropriate Hilbert space endowed with the standard inner product

$$\langle \boldsymbol{X}, \boldsymbol{Y} \rangle = \int_{\mathscr{D}} \boldsymbol{X}^* \, \boldsymbol{Y} \, \mathrm{d}\boldsymbol{x}, \tag{6}$$

where $\boldsymbol{X}$ and $\boldsymbol{Y}$ are any vector fields $\in \mathbb{C}$, $\mathscr{D}$ denotes the fluid domain, the asterisk denotes complex conjugation, and the induced norm is denoted by $||\cdot||$.

A. Resolvent and linear stability analyses

An increasingly popular way of analyzing flows is based on the resolvent operator. This way of linear analysis is treating the system under investigation as an input–output system and aims at describing the characteristics of the system by its response behavior to external forcing. While the global stability for a linear operator is based on an initial-value problem formalism of an evolving flow field, the resolvent framework casts the same problem in the frequency domain, often accomplished by a Laplace transform. The rationale behind resolvent and linear stability analyses is that any linear operator has a unique footprint in the complex plane. This way, the operator behavior can be understood by considering certain sets in the complex plane as stated by Trefethen and Embree (2005).

Due to the symmetries of the problem, for further analysis, we assume the Fourier–Laplace representation.

$$\boldsymbol{z}'(t, r, \theta, z) = \hat{\boldsymbol{z}}_{km}(r; s) e^{\mathrm{i}(m\theta + k z - s t)} + \text{c.c.}, \tag{7}$$

where $m \in \mathbb{Z}$ and $k \in \mathbb{R}$ are the nondimensional azimuthal and streamwise wavenumbers, respectively, $\mathrm{i} = \sqrt{-1}$, and $s = \omega + \mathrm{i}\,\sigma \in \mathbb{C}$ is the complex frequency. For a given value of the *complex* frequency s, the *complex* amplitudes of the state of the system $\hat{\boldsymbol{z}}_{km}$ are functions of the radial coordinate, r. If forcing is null ($\boldsymbol{f}(\boldsymbol{x}, t) = \boldsymbol{0}$), the linearized nondimensional Navier–Stokes equations (3) can be written (Fabre *et al.*, 2006) in matrix form as

$$-\mathrm{i}\, s\, \boldsymbol{I}\, \hat{\boldsymbol{z}}_{km} = \left(-\boldsymbol{L} + \frac{1}{Re}\boldsymbol{L}_\nu\right)\hat{\boldsymbol{z}}_{km}, \tag{8}$$

where the matrices $\boldsymbol{I}$, $\boldsymbol{L}$, and $\boldsymbol{L}_\nu$ are explicitly written in Appendix A.

Since the selected base flow has no free parameter, for a prescribed Reynolds number, Re, and a given pair of (k, m), Eq. (8) constitutes a generalized eigenvalue problem for solving the complex frequencies s_ℓ and the spatial structure of the modes (eigenvectors) $\hat{\boldsymbol{z}}_{km}$ for $\ell = 1, 2, \ldots$. The real part of the frequency, ω, is the oscillation rate of the wave, and the imaginary part σ, which is always negative here, corresponds to its damping rate. The problem can be numerically simplified eliminating the pressure and the axial velocity perturbation fields from the system (Mao and Sherwin, 2012).

By replacing (7) in (4), we obtain the following expression:

$$\begin{aligned} \hat{\boldsymbol{z}}_{km}(s) &= \boldsymbol{C}(\mathrm{i}s\boldsymbol{I} - \boldsymbol{A}_{km})^{-1}\boldsymbol{B}\hat{\boldsymbol{f}}_{km}(s), \\ \iff \quad \hat{\boldsymbol{z}}_{km}(s) &= \Re(s; \boldsymbol{A}_{km})\hat{\boldsymbol{f}}_{km}(s), \end{aligned} \tag{9}$$

where $\Re(s; \boldsymbol{A}_{km}) := \boldsymbol{C}(\mathrm{i}s\boldsymbol{I} - \boldsymbol{A}_{km})^{-1}\boldsymbol{B}$ denotes the resolvent (Schmid, 2007; Blanco-Rodríguez *et al.*, 2016; and Bölle *et al.*, 2021). From this definition, resolvent analysis aligns itself with the familiar concept of a transfer function, widely applied in control theory. Canonical decomposition of the resolvent $\Re(s; \boldsymbol{A}_{km})$ (dropping explicit dependence on k, m for convenience)

$$\Re(s; \boldsymbol{A})\hat{\boldsymbol{f}}(s) = \sum_{i=1}^{N} \mu_i(s)\boldsymbol{v}_i(s)(\boldsymbol{w}_i(s), \hat{\boldsymbol{f}}(s)) \tag{10}$$

07 March 2025 08:03:06

© Author(s) 2025

yields a hierarchy of orthogonal modes $(\boldsymbol{v}_i(s), \boldsymbol{v}_j(s)) = (\boldsymbol{w}_i(s), \boldsymbol{w}_j(s)) = \delta_{ij}$ such that $\mu_1(s) \geq \mu_2(s) \geq \cdots \geq \mu_N(s) > 0$. Physically, for any given frequency s, $\boldsymbol{w}_i$ constitutes the optimal spatial forcing pattern yielding the corresponding response pattern $\boldsymbol{v}_i$ with the amplification μ_i. The first value $\mu_1(s)$ is identical to the operator norm of the resolvent $||\Re(s;\boldsymbol{A})||$ at the same frequency.

In Eq. (9), we tacitly assumed the operator inversion to be possible. This is in fact true only for a subset of the complex plane called *resolvent set* $\rho(\boldsymbol{A}) \subset \mathbb{C}$. The set complement $\sigma(\boldsymbol{A}) := \mathbb{C}\backslash\rho(\boldsymbol{A})$ is called *spectrum*, controlling asymptotic linear stability. We note that for a linearly stable system as the Lamb–Oseen vortex is (Fabre *et al.*, 2006), $i\mathbb{R} \subset \rho(\boldsymbol{A})$, that is, the resolvent is defined on the entire imaginary axis, i.e., for purely harmonic forcing as in Bölle *et al.* (2021).

This dichotomy of the complex plane actually allows for a direct physical interpretation. The impossibility of inversion in (9) precisely occurs if the frequency s is identical to an eigenfrequency of the system, in other words, in the case of resonance. Importantly, if the dynamics is non-normal as is the case for vortices shown by Antkowiak and Brancher (2004) and Bölle *et al.* (2021), significant amplification is possible even far away from any eigenvalue. Trefethen *et al.* (1993) called this phenomenon *pseudoresonance*. Generally, it can be shown that

$$\frac{1}{d(s,\sigma(\boldsymbol{A}))} \leq ||\Re(s;\boldsymbol{A})|| \quad \forall s \in \rho(\boldsymbol{A}), \tag{11}$$

where $d(s,\sigma(\boldsymbol{A})) := \min_{\lambda\in\sigma(\boldsymbol{A})}|s-\lambda| > 0$ defines the distance of s from the closest eigenvalue, λ, in the spectrum. Equality in (11) holds if and only if the linear operator $\boldsymbol{A}$ is normal. The left-hand expression in (11), obviously corresponding to the classical resonance condition, describes the system dynamics as it was due to a normal operator. Thus, actual inequality in (11) directly indicates those frequency ranges for which the dynamics is truly affected by non-normality. This frequency dependence was termed selective non-normality in Bölle *et al.* (2021).

B. Frequency response

We also study here the linearized forced Navier–Stokes equations in a Lamb–Oseen vortex from an input–output point of view (Jovanović, 2021) by analyzing their spatiotemporal frequency responses. Spatially distributed and temporally varying body force fields are considered as inputs, and components of the resulting velocity field are considered as outputs into these equations. As far as the authors know, the use of the frequency response to determine the particular solution of the temporal evolution of a disturbance in a stable system such as the Lamb–Oseen vortex with a spatially prescribed force was first proposed by Blanco-Rodríguez *et al.* (2016), assuming an external volumetric body force in the form of a pulsating off-axis axisymmetric jet with a Gaussian radial profile. This forcing is referred to as single-point injection (SPI) and constitutes a generic model for jet–vortex interaction with possible applications in contrail formation and active control. In this study, we assume a variable radial offset $a_f \geq 0$ with respect to the vortex center. In the frequency response framework, we assume a rectangular Cartesian grid and use the Fourier series ansatz

$$\boldsymbol{q}'(t,x,y,z) = \hat{\boldsymbol{q}}_{k_x,k_y,k_z}(t)e^{i\boldsymbol{k}\cdot\boldsymbol{x}} + \text{c.c.} \tag{12}$$

The general solution of (4) in the time domain reads as follows:

$$\boldsymbol{z}'(t) = \boldsymbol{C}e^{t\boldsymbol{A}}\boldsymbol{q}_0 + \int_0^t \mathrm{d}\tau\, \boldsymbol{C}e^{(t-\tau)\boldsymbol{A}}\boldsymbol{B}\boldsymbol{f}(\tau). \tag{13}$$

In the frequency response analysis, we assume jet-like harmonic non-dimensional volumetric forcing

$$\boldsymbol{f}(\boldsymbol{x},\, t) = \frac{1}{2}w_f(\boldsymbol{x})\, e^{i\omega_f t}\boldsymbol{e}_z + \text{c.c.} = w_f(\boldsymbol{x})\, \cos(\omega_f t)\boldsymbol{e}_z, \tag{14}$$

in the streamwise velocity component of Eq. (4). Herein, ω_f is the actuation frequency and $w_f(\boldsymbol{x}) \in \mathbb{R}$ determines the spatial shape of the forcing. In particular, we depict in Fig. 2(a) an SPI, defined by the Gaussian

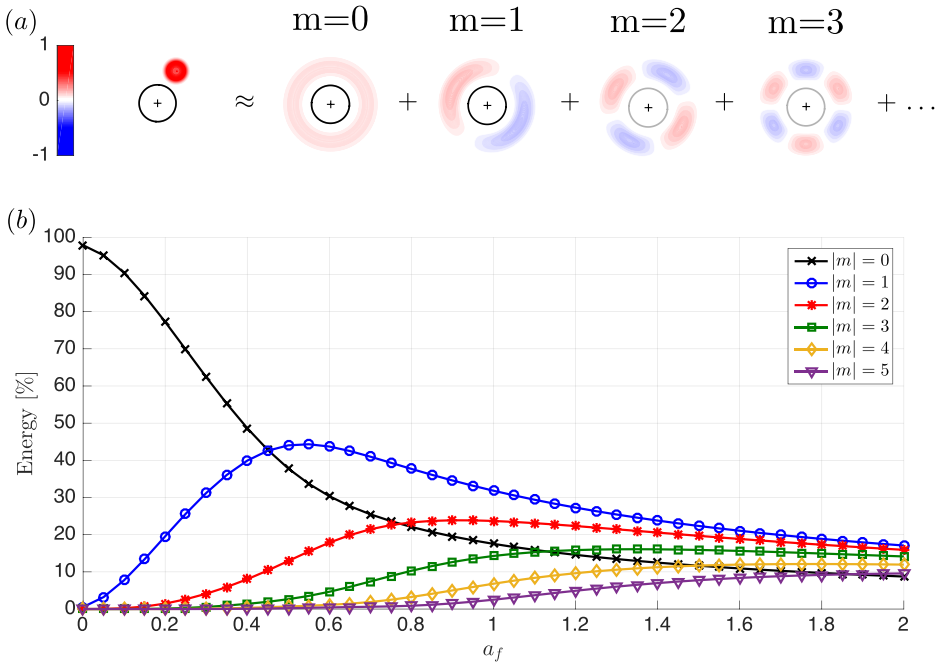

FIG. 2. (a) Fourier (real) decomposition (first four modes) of the SPI spatial structure ($a_f = 2$). (b) Energy contribution, E_m/E_f (see Appendix B), of the first six azimuthal Fourier modes for an SPI forcing, for varying injection distances a_f.

07 March 2025 08:03:06

© Author(s) 2025

$$w_f(x,y) = e^{-\beta\left((x-x_c)^2+(y-y_c)^2\right)}, \tag{15}$$

where $(x_c, y_c) = a_f(\cos(\theta_c), \sin(\theta_c))$. This is a generic form of an isotropically spreading jet having reached the self-similar regime starting from a true point source described by Tennekes and Lumley (1978). This jet profile also corresponds to jet flows observed in experiments of the same type of setup undertaken experimentally by Bölle *et al.* (2023).

The spatial structure of an SPI with a forcing distance $a_f = 0$ is purely axisymmetric, whereas for $a_f \neq 0$ the SPI has an intricate modal decomposition. Figure 2(a) shows the azimuthal mode decomposition for an SPI with $a_f = 2$, and Fig. 2(b) represents the energy distribution of the azimuthal modal decomposition as a_f is varied from 0 to 2. While the axisymmetric mode $m = 0$ is dominant for $a_f < 0.3$, the helical mode $|m| = 1$ prevails for larger forcing distances. The azimuthal components with $|m| > 1$ are also present for $a_f > 0$; however, none of them is the dominant energetic mode in the analyzed region of a_f.

To perform our numerical study, we set the spreading parameter of the forcing to $\beta = 10$. This chosen value is one such that the relative size of the SPI forcing is of the same order of magnitude as the vortex core. Nevertheless, the mode response of the Lamb–Oseen vortex is not critically dependent on this value. Due to azimuthal symmetry, we apply the forcing at the fixed but arbitrary angle $\theta_c = \pi/3$ with respect to the horizontal, as depicted in Fig. 2(a).

We compute the gain of integral fluctuation kinetic energy in the whole domain due to the applied forcing by the ratio

$$G(\omega_f, t) = \frac{E(t)}{E_f(t=0)} = \frac{\langle \boldsymbol{u}', \boldsymbol{u}' \rangle}{\langle \boldsymbol{f}(\boldsymbol{x},0), \boldsymbol{f}(\boldsymbol{x},0) \rangle} = \frac{\int_{\mathscr{D}} (u'\,u'^{*} + v'\,v'^{*} + w'\,w'^{*})\,\mathrm{d}\boldsymbol{x}}{\int_{\mathscr{D}} w_f^2\,\mathrm{d}\boldsymbol{x}}. \tag{16}$$

We define $G_\infty(\omega_f) := G(\omega_f, t \to \infty)$ as the stationary value of $G(\omega_f, t)$ where we take at least $t = \Omega_c\, T = 1000$ in our simulations to ensure that an oscillating but converged state is reached. After convergence is achieved, G_∞ is calculated averaging the values of the last 5% of the temporal signal. Bernoff and Lingevitch (1994) analyzed the relaxation of a perturbed Gaussian vortex finding that perturbations evolve on a $Re^{1/3}$ timescale which corresponds to $t_{pert} \approx 20 \ll 1000$ for our case.

We solve (13) numerically, using the numerical tool developed in Blanco-Rodríguez *et al.* (2016), which is based on the Fourier-based pseudospectral discretization given in Delbende *et al.* (1998). The linearized equations are solved in the Fourier space for a rectangular periodic domain $\mathscr{D} = [-L_x/2, L_x/2] \times [-L_y/2, L_y/2]$, with a discretization of 256×256 equispaced collocation points on a cartesian grid for $L_x = L_y = 12\,R_0$. The time step $\delta t = \Omega_c\,\delta T = 0.01$ is chosen to satisfy the Courant–Friedrichs–Lewy (CFL) condition. These numerical parameters are chosen so that a proper convergence is achieved without incurring in an excessive computational burden. More details concerning the numerical implementation can be found in Blanco-Rodríguez *et al.* (2016), where Table A2 in Appendix A includes a sensitivity analysis for the number of spatial collocation points and the convergence of the gain for long time simulations.

III. RESULTS OVERVIEW

First, we analyze the energy gain obtained from the frequency response for an SPI at different forcing distances, a_f. Figure 3 represents the standard logarithm for long time gains ($\log_{10} G_\infty$), for every (ω_f, k) pair, and for $a_f = 0$, 0.5, 1, and 2. Remarkably, most of the (ω_f, k) pairs with significant gain levels are located in the least damped mode branches [also named dispersion relations in Le Dizès and Lacaze (2005)] obtained by linear stability analysis. These branches, depicted in dashed–dotted and dashed lines, correspond to axisymmetric ($m = 0$) and helical modes ($|m| = 1$), respectively. The branches are labeled in (a) and (b) as proposed by Fabre *et al.* (2006) for consistency.

In the case of $a_f = 0$, see Fig. 3(a), the maximum gain points are located exclusively in axisymmetric mode branches. For this particular case, the energy contribution of the non-axisymmetric components is mainly residual and close to 0 (see Fig. 2). As a result, they cannot excite the non-axisymmetric modes which do arise when the non-axisymmetric $m = 1$ component is not negligible for $a_f > 0$. This fact constitutes the main reason why an SPI forcing aligned with the vortex axis results in maximum gains on the axisymmetric ($m = 0$) branches. In particular, we find three different axisymmetric branches that correspond to $m = 0$, a, b, and c. The structure of the modes from the $m = 0$, a branch presents a single lobe concentrated axisymmetrically in the vortex core, whereas $m = 0$, b modes present two axisymmetric structures with alternating signs and, consequently, $m = 0$, c modes have three of them. The highest gain is obtained for the $m = 0$, a branch, presenting a maximum value that is at least two orders of magnitude higher than those corresponding to the b and c branches.

For a forcing with $a_f > 0$, the SPI structure is no longer axisymmetric, resulting in more intricate flow dynamics. Focusing on the gain map of $a_f = 0.5$, we can observe in Fig. 3(b) the presence of zones of high gain associated with damped helical waves $m = 1$ from linear stability analysis. Note also that the $m = 0$ branches are still present as expected, since the non-axisymmetric SPI forcing shows a non-null presence of the $m = 0$ component at $a_f = 0.5$, as shown in Fig. 2(b). On the other hand, three families of helical waves can be distinguished for the case $a_f = 0.5$, referred to as C, D, and L in the gain map. While the spectrum admits multiple branches for each kind, we only show the least damped in the gain map.

Frequency response analysis for $a_f = 1$ and $a_f = 2$ also displays zones with high gain corresponding to both $m = 0$ and $m = 1$ branches. However, for $a_f = 2$ the $m = 1$, C branch is not significant. This fact is not unexpected since the structure of the modes contained in this branch is located entirely in the vortex core, and an injection further from the vortex core hinders its excitation. Note also that the exact value of the Reynolds number does not significantly affect the general structure for the gain map. Figure 3(d) is very similar to the results of Blanco-Rodríguez *et al.* (2016) obtained for $a_f = 2$ and $Re = 5000$.

The presence of the aforementioned high gain modes can be explained by a forced resonance mechanism: the harmonic SPI forcing induces a perturbation field that excites diverse Kelvin waves of

07 March 2025 08:03:06

© Author(s) 2025

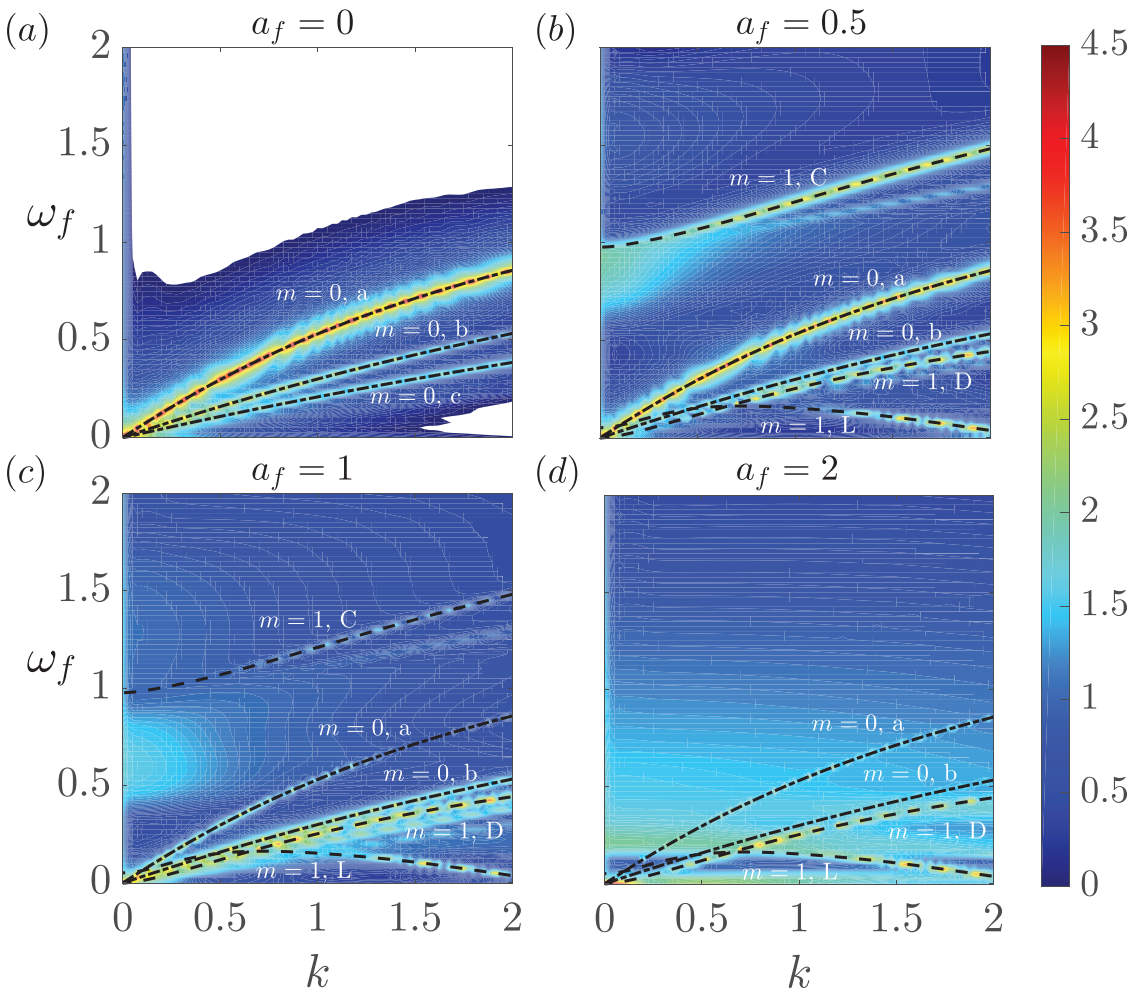

FIG. 3. $\log_{10}(G_\infty)$ gain maps obtained by frequency response analysis for four different forcing distances: (a) $a_f = 0$, (b) $a_f = 0.5$, (c) $a_f = 1$, and (d) $a_f = 2$. White regions in panel (a) represent input parameters for which $G_\infty < 1$. Each map contains 81×81 equispaced numerical experiments in the (k, ω_f) plane. Note that the colorbar was set to a maximum of $\log_{10}(G_\infty) = 4.5$ for visualization purposes, but there exist some values up to $\log_{10}(G_\infty) \approx 4.9$ located in the $m = 0$, *a* branch for $a_f = 0$. Some of the most amplified LS mode branches are superposed in dashed–dotted ($m = 0$) and dashed lines ($m = 1$) for axisymmetric and helical modes, respectively.

the Lamb–Oseen vortex. This hypothesis was initially validated by Antkowiak (2005), who effectively compared it with a basic model of a forced harmonic oscillator. By selecting an appropriate forcing term to accurately reflect the impact of the chosen mode, the frequency of this forcing term was found to match closely with those of the selected waves. From this fundamental harmonic oscillator model, an estimate of the energy amplification for large times can be derived: $G_\infty = ((\omega_f - \omega)^2 + \sigma^2)^{-1}$, where σ represents the damping rate of the eigenmode of the system. From this estimation of energy growth, it is evident that the selection process relies on two criteria. First, the disturbance should be in phase with the wave to ensure continuous excitation, thereby minimizing the $(\omega_f - \omega)$ term. Second, selecting one of the least damped waves minimizes the σ term, facilitating a maximal energy amplification. Pradeep and Hussain (2006) performed a similar analysis on a Rankine vortex, finding evidence of a resonance-driven excitation of vortex waves.

Finally, it is important to note that linear stability analysis is not sufficient to capture all high gain excitations shown in Fig. 3. In particular, two relevant zones are not accounted for. The first one is located at very low k and $0.7 < \omega_f < 1$ for $a_f = 0.5$ and it is persistent in $a_f = 1$ and $a_f = 2$ for lower ω_f values. Specifically, $0.45 < \omega_f < 0.8$ for $a_f = 1$ and $0.2 < \omega_f < 0.7$ for $a_f = 2$. For these three values of a_f, the axial velocity perturbation presents a helical ring structure, with a radius that depends directly on the forcing distance a_f and ω_f. We focus first on the region of $0.45 < \omega_f < 0.8$ for $a_f = 1$, see Fig. 4(a). For any of these (ω_f, k) points, the frequency response results display a spiral structure appearing as a ring further from the vortex core, which occurs in the vicinity of critical points r_c, which are related to the forcing of a viscous critical layer. These critical points are defined as the radial position at which a change of sign occurs and are related to the frequency. For the sake of clarity, we represent in Fig. 4(b) the relation between ω/m and r_c described by Le Dizès (2004). We have

07 March 2025 08:03:06

© Author(s) 2025

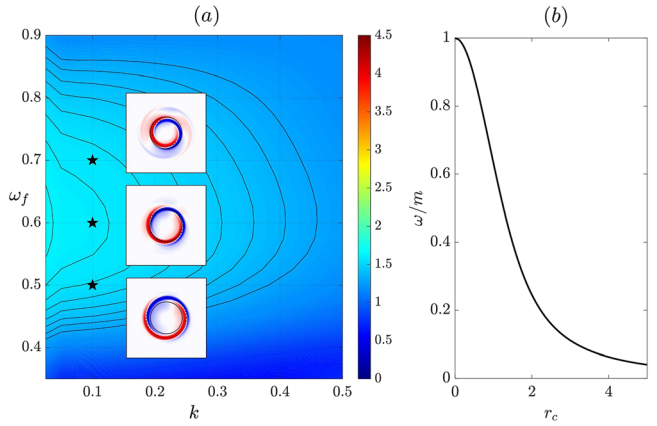

FIG. 4. (a) Zoom of the $\log_{10}(G_\infty)$ map for $a_f = 1$, with axial velocity field (real part) insets in high gain areas (marked with stars) for $k = 0.1$ and $\omega_f \in \{0.8, 0.6, 0.2\}$ for region 1, respectively. (b) Critical points, r_c, of the Lamb–Oseen vortex as a function of the frequency, ω/m, for $m \geq 1$. Panel (a) contains eight contour levels from 1.3 to 1.65 in steps of 0.05.

selected three points with different ω_f to illustrate how their changes in sign correspond with the r_c predicted position, see again Fig. 4(a). As explained below, small variations of k within the long-wavelength regime do not alter the structure or the radius of the ring-like helical perturbation.

Figures 5(a)–5(c) represent three subplots of the aforementioned structures at different a_f to illustrate their similarities in the same area of long-wavelength regime, with the main difference residing in the radius of the ring-like helical structure. Thus, these regions of high gain just described for $a_f = 1$ are also present in the cases of $a_f = 0.5$ and $a_f = 2$ but for different ω_f. These modes are only excited by the forcing at a proper location a_f near to the critical radius of the structure, r_c, being $\omega = m\,\Omega(r_c)$. This relation infers a direct link between the critical radius, r_c (or a_f) and the frequency ω as $\frac{\omega}{m} = \frac{1}{r_c^2}(1 - e^{-r_c^2})$ [see Fig. 4(b)].

This fact is consistent with the area of high gain having lower ω_f with increasing a_f (and associated with r_c). On the other hand, Fig. 5(d) shows the flow pattern of the second region that is only visible for the case of $a_f = 2$ and it is located in the region of short-wavelength regime above the $m = 1$, L branch. Although its resulting excitation presents again the outer ring structure at $a_f = 2$ with a size similar to the r_c, its structure is more complicated since the vortex core presents other disturbances not observed in the first region. In addition, this value of $k = 1.625$ the second region is close to that at which the transient energy growth presents a maximum gain for $m = 1$ for $Re = 5000$. In particular, Antkowiak and Brancher (2004) reported that the disturbances that experience the most growth take the form of concentrated spirals at the outer periphery of the vortex which rapidly excite bending modes within the vortex core. Our frequency response results are in agreement, displaying the same flow patterns depicted in Fig. 5(d).

We next turn our attention to a possible physical explanation of the areas with relevant gains that are not captured by the linear stability analysis. For this purpose, we leverage the resolvent analysis, that allows to compute the maximum gain for a given triad (ω, k, m). Figure 6 shows (ω, k) contour maps of the standard logarithm of the resolvent $[\log_{10}(\Re)$, see Eq. (10)] for $m = 0$ (a) and $m = 1$ (b). LS branches for $m = 0$ and $m = 1$ are superposed to the panels (c) and (d), respectively to facilitate their comparison. We observe in Fig. 6(a) common areas with linear stability branches $m = 0$, a and $m = 0$, b and to a lesser extent $m = 0$, c. These areas were also obtained in the gain map for $a_f = 0$ [see again Fig. 3(a)]. Specifically, a maximum of $\Re \approx 10^3$ and a peak of $G_\infty = 10^{4.9}$ corresponds to the $m = 0$, a branch. Additionally, there is an area with high gain for $\omega_f < 0.05$. However, combining such a low frequency with the condition of zero net mass flow presents significant challenges. Achieving this would necessitate an exceedingly long implementation period, which approaches the limits of the validity of the mathematical implementation of the frequency response analysis. For $m = 1$, the region corresponding to the $m = 1$, C branch is clearly visible with a local maximum of $\Re \approx 10^{2.35}$, but the highest value of $\Re \approx 10^{4.74}$ is located in the region with low ω and high k corresponding to the $m = 1$, L branch. The results obtained from the resolvent analysis are not restricted by a particular a_f value. However, the radial position of the optimal forcing obtained influences the modes contained in its azimuthal structure as described in Fig. 2(b) and, therefore, the possible modes that are excited in the results. This connection is elaborated further in Sec. IV C.

Additionally, the ratio $(\Re/d^{-1})$, presented previously in Eq. (11) is commonly used as a non-normality criterion in vortex dynamics, see for instance Blanco-Rodríguez *et al.* (2017) and Bölle *et al.* (2021). Figure 6 bottom panels present two contour maps $\log_{10}(\Re/d^{-1})$ for the first two azimuthal wavenumbers $m = 0$ (c) and $m = 1$ (d). The

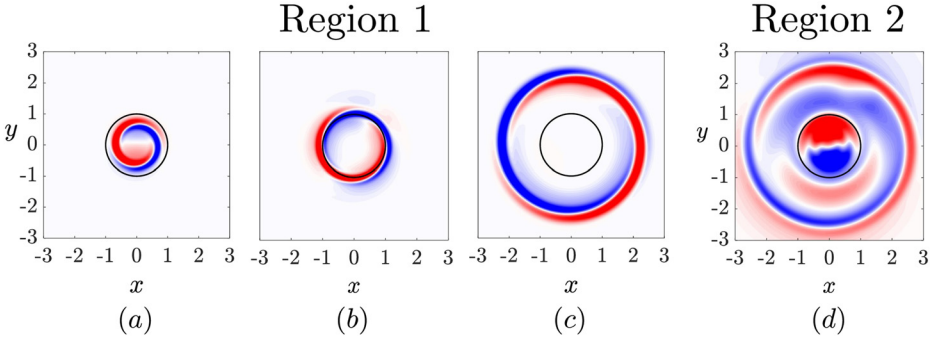

FIG. 5. Axial velocity field (real part) in high gain regions not obtained from the excitation of linear stability branches. Region 1 with $k = 0.1$: (a) $a_f = 0.5, \omega_f = 0.8$, (b) $a_f = 1, \omega_f = 0.6$, and (c) $a_f = 2, \omega_f = 0.2$. Region 2 with $k = 1.625$: (d) $a_f = 2, \omega_f = 0.15$.

07 March 2025 08:03:06

© Author(s) 2025

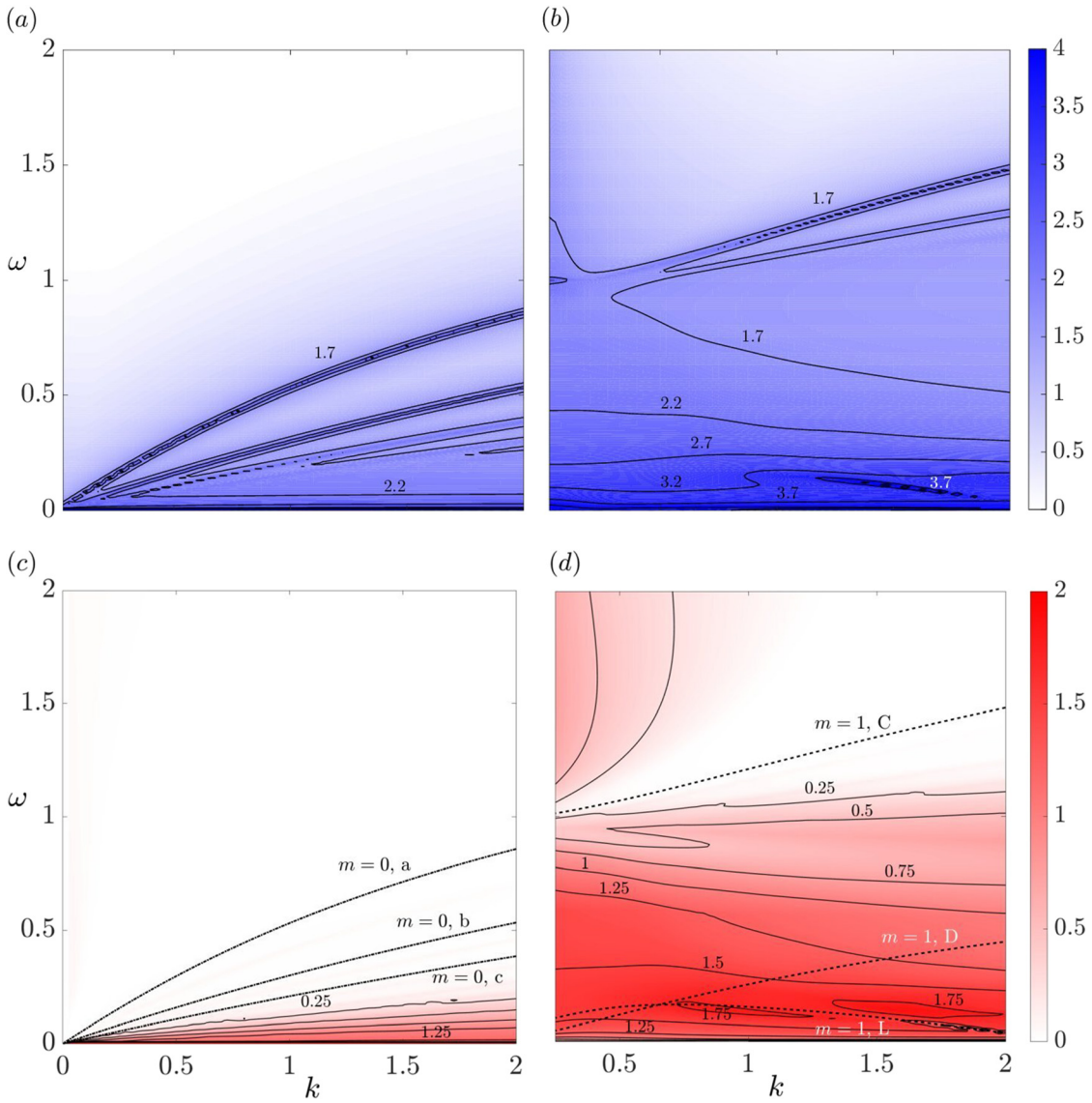

FIG. 6. Filled contour maps of the $\log_{10}(\Re)$ for (a) $m = 0$ and (b) $m = 1$ and contour maps of the $\log_{10}(\Re/d^{-1})$ for (c) $m = 0$ and (d) $m = 1$ from resolvent analysis. (ω, k) cases are computed in the range of $0 - 2$ with 200 equispaced points for ω and 81 for k. Panels (a) and (b) contain six contour levels from 1.7 to 4.2 in steps of 0.5, and panels (c) and (d) contain seven contour levels from 0.25 to 1.75 in steps of 0.25. Some of the most amplified LS mode branches for $m = 0$ (dashed–dotted lines) and $m = 1$ (dashed lines) are superposed to the panels (c) and (d), respectively.

non-normal effects present a contrasting distribution in the (ω, f) plane for both modes, showing higher values for the latter. For $m = 0$, the non-normal effects are confined to the area with very low ω and are negligible in the rest of the studied parameter space. The isocontours start at $k = 0$ and have their maximum at $k = 2$, e.g., the contour of $\log_{10}(\Re/d^{-1}) = 1.25$ has its maximum at $\omega \approx 0.015$. Therefore, capturing the non-normal effects with $m = 0$ in a practical implementation is highly complex, as it would necessitate an extremely low forcing frequency ω_f. However, $m = 1$ has several areas with strong non-normal effects, being the maximum $\log_{10}(\Re/d^{-1}) = 1.85$ located at $\omega \approx 0.14$ and $k \approx 1.55$, corresponding to the region above the $m = 1$, L branch of the linear stability analysis. We remind the reader that this value of k also corresponds to the peak gain in the transient energy growth given by Antkowiak and Brancher (2004) for a Lamb–Oseen vortex at $Re = 5000$ and $m = 1$. This non-normal region also coincides with the one with high gain in the top of the $m = 1$, L branch for $a_f = 2$ [see Fig. 3(d)]. Finally, the area with $k < 0.5$ and $\omega < 0.75$ also displays a strong non-normal component and can be related to the first area of high gain described in Fig. 3 for $a_f = 0.5, 1, 2$. In summary, comparing Figs. 3 and 6(a)–6(c), we do not find a direct relationship between the appearance of high-gain areas obtained from the frequency response results and their

07 March 2025 08:03:06

© Author(s) 2025

corresponding significant amplification from non-normal effects for axisymmetric modes ($m = 0$). However, for helical modes ($m = 1$), we observe regions where non-normal effects and high-gain are simultaneously highlighted, compare Figs. 3 and 6(b)–6(d), suggesting a link between the two phenomena that appear mostly for $a_f = 0.5$. As stated before, resolvent analysis in its standard form is not capable of including the dependence on a_f as a free parameter. Therefore, it is not expected that the first aforementioned region is well represented with its changing position for different a_f values, but it is very helpful to get an insight of its physical significance via the presence of strong non-normal effects.

IV. DETAILED STRUCTURAL MODE ANALYSIS

In the following, we structure the results pertaining to the different families of modes of each linear stability branch according to their azimuthal structure. We consider only two azimuthal wavenumbers in the frequency response analysis: $m = 0$, corresponding to axisymmetric modes, and $|m| = 1$, corresponding to helical or bending modes. The rest of modes $|m| > 1$ are not considered since their gain is not significant compared to the first two azimuthal wavenumbers, and for the injection distances a_f studied, as shown in Fig. 3.

For the reasons given above, we consider $k = 1.55$ in all the cases with the corresponding ω value for each branch. The rest of the results for different k values within the same branch, not shown, are consistent and robust along each branch.

A. Axisymmetric modes, m = 0

1. m = 0, a branch

We depict in Fig. 7 the frequency response gain for long times, G_∞, vs the SPI distance, a_f, in a solid line. The insets present the axial velocity perturbation field (real part) of three representative cases for an SPI forcing with a given a_f, marked with circles. This branch shows its highest gain for $a_f = 0$ and decreases up to $a_f = 1$ where it reaches its minimum and then increases again up to a local maximum at $a_f = 1.4$, after which it decreases monotonically. Both local maximum gain points correspond to $m = 0$ structures, whereas the minimum gain point does not. In general, for all the branches studied in this paper, the local maxima and minima of the G_∞ graph varying with a_f correspond to changes in the azimuthal structure of the frequency response.

The structure within the core region of these two highlighted maxima is very similar not only to the structure obtained from the linear stability analysis (bottom left), but also to that corresponding to the response of the resolvent analysis, presented on the bottom right of Fig. 7. The structure of the optimal forcing from resolvent analysis corresponds with an SPI forcing with $a_f = 0$. This result is not surprising,

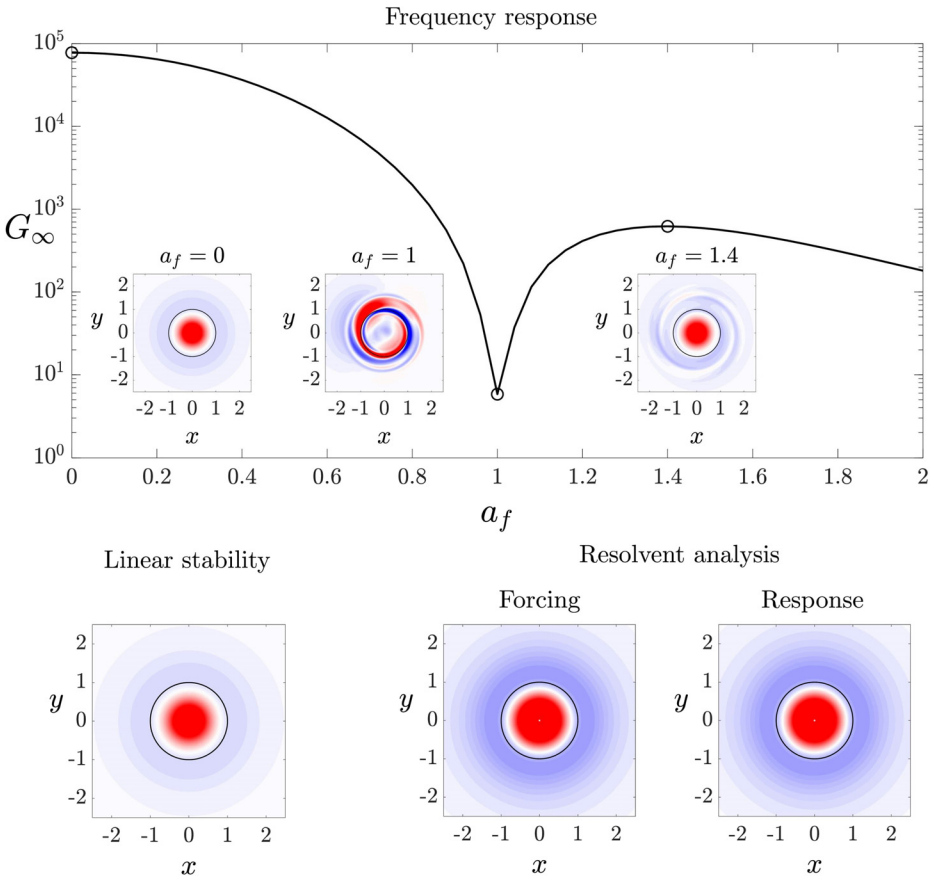

FIG. 7. $\mathbf{m = 0, a}$ branch; effect of the radial position a_f of an SPI forcing on the frequency response of the Lamb–Oseen vortex for $(k, \omega_f) = (1.55, 0.7293)$. The LS analysis ($m = 0$, $k = 1.55$) provides an eigenvalue complex frequency of $s = \omega + \sigma \mathrm{i} = 0.72937 - 1.3308 \times 10^{-3}\mathrm{i}$. The correspondence of both frequencies suggests that a resonance phenomenon is occurring. The axial component w' (real part) of the velocity perturbation field, $\boldsymbol{u}'$, from linear stability analysis, and the optimal forcing and optimal response from resolvent analysis is presented. All insets also depict the real part of the axial velocity perturbation. Red and blue hues correspond to positive and negative values, respectively.

07 March 2025 08:03:06

© Author(s) 2025

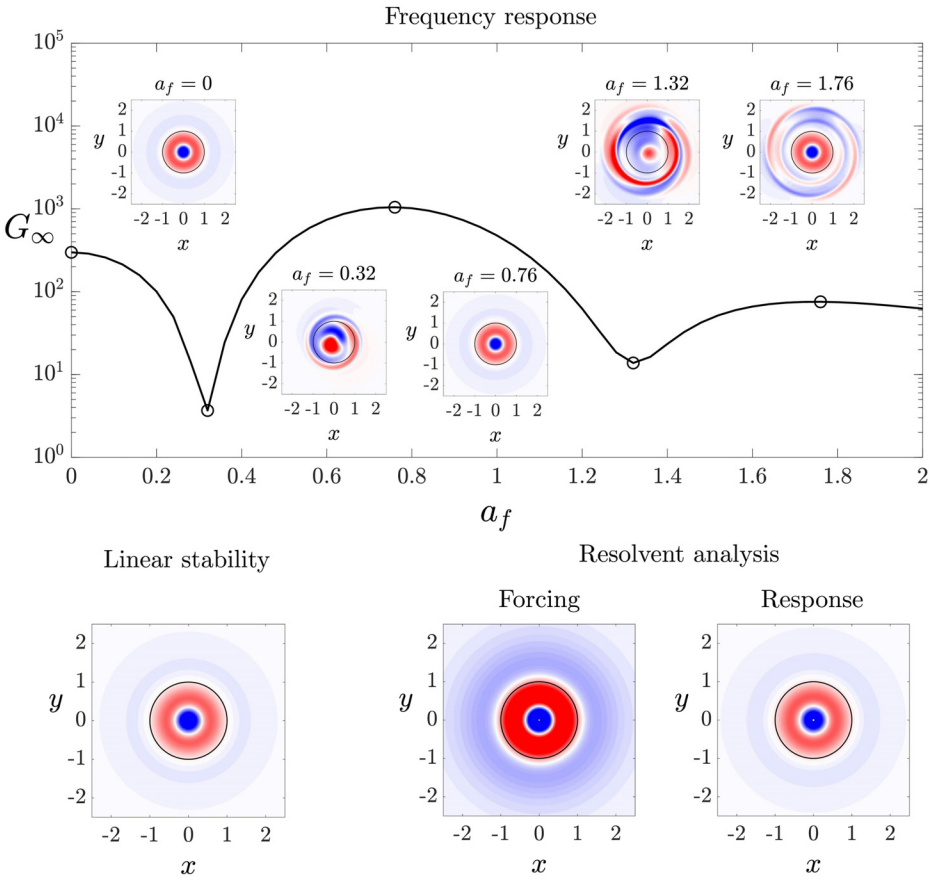

FIG. 8. As in Fig. 7, but for the case $\mathbf{m = 0, b}$ branch, where $(k, \omega_f) = (1.55, 0.4355)$ and LS analysis provides $s = \omega + \sigma\,\mathrm{i} = 0.43553 - 3.611 \times 10^{-3}\mathrm{i}$.

since the axisymmetric SPI forcing presents the maximum value of the frequency response gain. However, it is very interesting to remark how the local maximum at $a_f = 1.4$ recovers the structure of the optimal gain with a $m = 0$ structure through a non-axisymmetric forcing, even though its amplitude is smaller than the case for $a_f = 0$.

2. m = 0, b branch

As shown in Fig. 8, the characteristic structure of this linear stability branch is an axisymmetric structure with two sign-alternating lobes inside the vortex core. This flow pattern is also recovered in the optimal response structure obtained from the resolvent analysis and in the frequency response analysis result for $a_f = 0$. Additionally, a significant novel finding is that a non-axisymmetric forcing can also recover this two-lobed structure. In particular, for $a_f = 0.76$, there is a maximum gain point which corresponds to approximately 3.5 times the gain value for $a_f = 0$, presenting the same structure. Therefore, even though the optimal forcing obtained from the resolvent analysis is axisymmetric, the frequency response analysis selects as the optimal forcing (based on the maximum gain criterion) an SPI forcing displaced from the vortex center. It is important to note that this axisymmetric structure is recovered for a wide range of a_f, $0.5 < a_f < 1.6$, see again top of Fig. 8, enabling its implementation in an experimental setup feasible.

In addition, linear stability and frequency response results are in agreement. The $m = 0$, a branch has a higher ω and lower damping rate σ than the $m = 0$, b branch (compare $0.72937 - 1.3308 \times 10^{-3}\mathrm{i}$ vs $0.43553 - 3.611 \times 10^{-3}\mathrm{i}$), which makes the former closer to being the most unstable within this stable regime. This is also the case for the gain maps, where the $m = 0$, a branch usually has a higher gain than the $m = 0$, b branch (see Fig. 3), except for a narrow region close to $a_f = 1$ (compare Figs. 7 and 8).

Finally, there are two minima located at $a_f \approx 0.32$ and $a_f \approx 1.3$. As happened in the $m = 0$, a branch, the former is again characterized by a change in the flow pattern near the vortex periphery, while the latter case that is followed by a plateau in the peak gain at $a_f \approx 1.76$ with intricate structures: an axisymmetric mode structure in the center surrounded by a combination of $m = 1$ and $m = 2$ perturbations.

3. m = 0, c branch

The characteristic structure of this linear stability branch is an axisymmetric structure with three sign-alternating lobes inside the vortex core as described above. This structure is also recovered by the frequency response analysis for $a_f = 0$, and from the resolvent analysis (see Fig. 9). Therefore, this is the third example for which the optimal response is achieved through an SPI that has a simpler structure than the optimal forcing.

07 March 2025 08:03:06

© Author(s) 2025

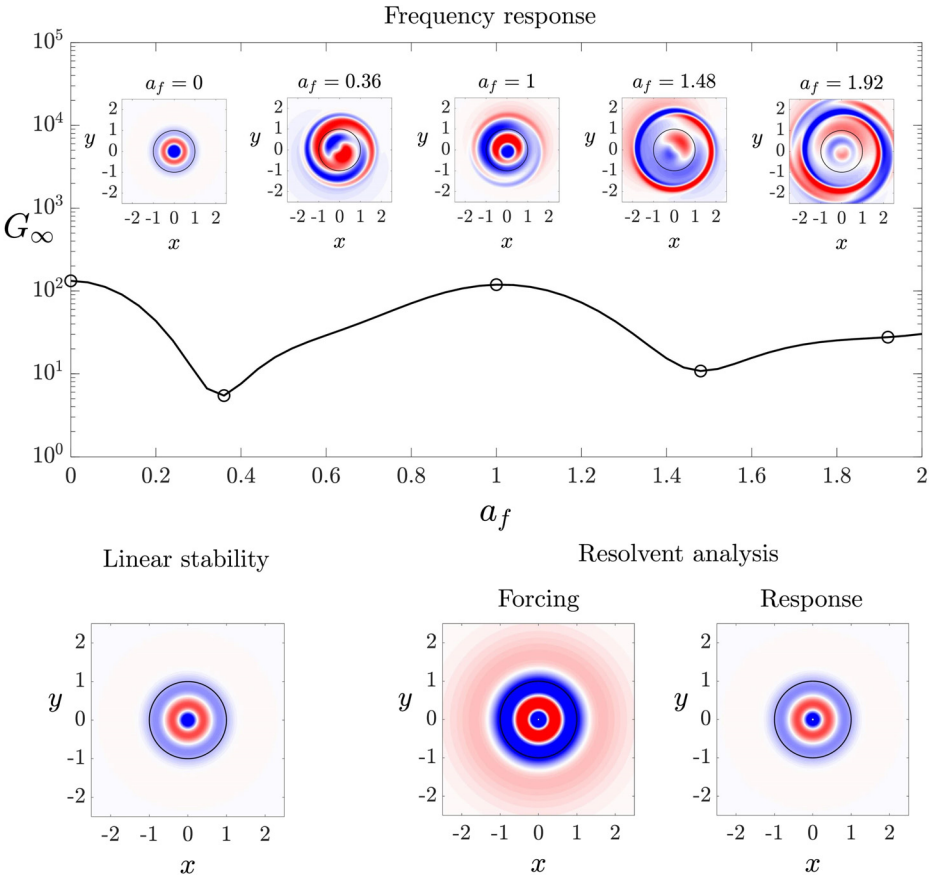

FIG. 9. As in Fig. 7, but for the case $\mathbf{m} = \mathbf{0}, \mathbf{c}$ branch, where $(k, \omega_f) = (1.55, 0.3088)$ and LS analysis provides $s = \omega + \sigma \mathrm{i} = 0.30878 - 7.1364 \times 10^{-3}\mathrm{i}$.

The second maximum of Fig. 9 corresponds to a value of $a_f = 1$ and has roughly the same gain value obtained from $a_f = 0$. As the radius increase, there is a symmetry breakdown at $a_f = 1$ and $a_f = 1.92$. Nevertheless, this is another example of a high gain obtained for an axisymmetric branch using a (non-symmetric) SPI forcing.

B. Helical modes, m = 1

1. m = 1, C branch

When an offcentered $a_f > 0$ SPI forcing is considered in the frequency response analysis, several $m = 1$ branches appear in the (k, ω_f)-plane. A first family of core waves obtained from linear stability is composed of dipoles with their main structure confined in the vortex core. These modes have not been observed in realistic vortex flows, and the reason may be that their structure is entirely located within the vortex core, being invisible from the outside of the vortex. In addition, the structure of the frequency response and linear stability analysis changes dramatically for very low values of k (long-wavelength regime), showing a convoluted rolled up ring structure (not shown). This change in structure related to the transition from inviscid center-modes to viscous center-modes has been observed around $k \approx 0.35$, which is consistent with asymptotic analysis that locates this change in behavior around $k \approx O(Re^{1/4})$, as reported by Fabre and Le Dizès (2008).

The maximum frequency response gain is obtained at $a_f \approx 0.5$, and the structure of the solution is similar to the optimal response (see Fig. 10). Hence, and again, an offcentered SPI is able to recover the same optimal output structure of the resolvent analysis but with a simpler implementation of the forcing.

For $a_f > 1.2$, more complex structures emerge, but their lower gain value (two orders of magnitude lower than the maximum) makes them unsuitable. Note also that the axisymmetric structure found for $a_f = 0$ is represented just for completeness, but it is not relevant for this branch. Only a non-axisymmetric forcing with $a_f > 0$ can present an $m = 1$ component and, therefore, be able to excite helical waves. For this reason, minimum gain solutions at $a_f = 0$ and their structure are not represented for the other $m = 1$ branches. In this case, the minimum gain level is again accompanied by a structural change at the vortex periphery, resulting in the emergence of a weak central mode with $m = 2$ in the vortex core when $a_f = 1.2$.

2. m = 1, D branch

Our numerical FR code finds a resonance with a $m = -1$ branch corresponding to the $m = 1$, D branch since there exists a correspondence between $\omega(m, k) = -\omega^*(-m, k)$ (Fabre *et al.*, 2006). The most noticeable characteristic of these modes is the robustness in the frequency response gain results, presenting a considerably high value of the gain for a large range of a_f, a feature that positions this mode as

07 March 2025 08:03:06

© Author(s) 2025

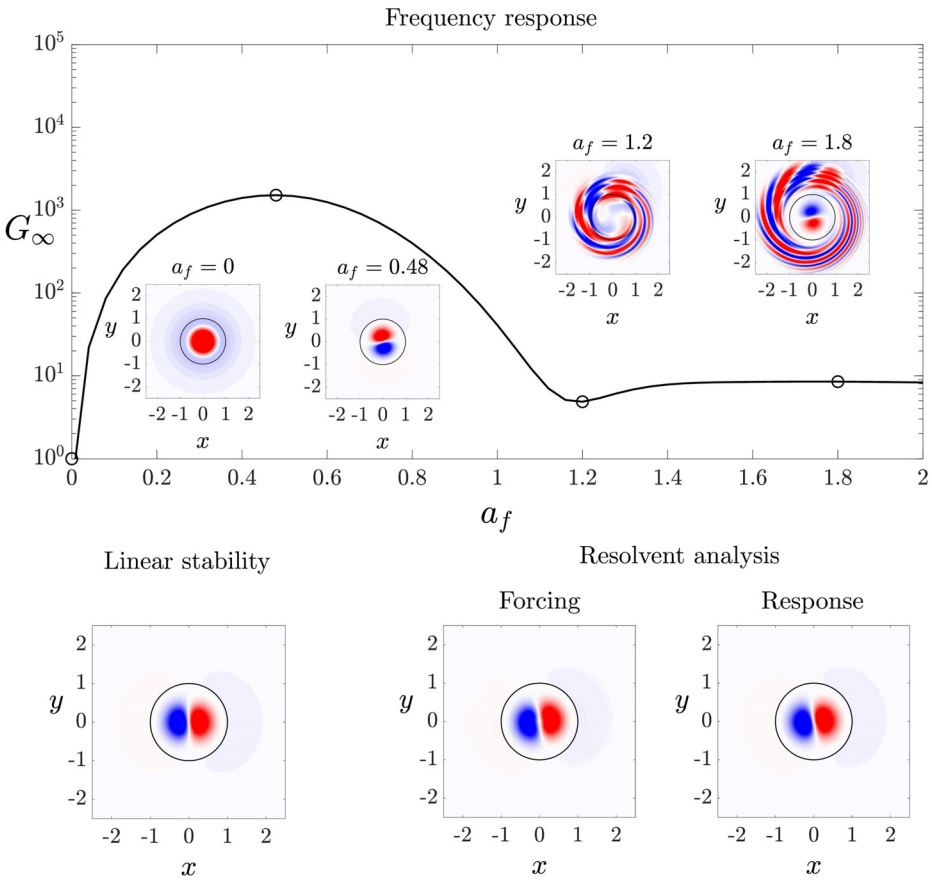

FIG. 10. As in Fig. 7, but for the case $\mathbf{m = 1, C}$ branch, where $(k, \omega_f) = (1.55, 1.3661)$ and LS analysis provides $s = \omega + \sigma\,\mathrm{i} = 1.3661 - 4.2931 \times 10^{-3}\mathrm{i}$.

the potential candidate to be most easily found in a experimental implementation. For any $a_f > 0$, the outer dipolar structure remains present (Fig. 11), even though at large forcing distances the shape of the response becomes increasingly disturbed. The maximum gain is obtained at $a_f = 0.92$ and presents a large effective a_f window with high gain. The solution obtained from the resolvent analysis and linear stability analysis also presents the same structure as the frequency response analysis. Finally, it is worth mentioning that this $m = 1$, D branch has the lowest linear stability damping rate σ of all the branches considered, closely followed by the $m = 1$, L branch (to be described in Sec. IV B 3). This fact suggests that the nature of these (displacement) disturbances makes them good candidates for practical applications aimed at reducing vortex strength.

3. m = 1, L branch

The representative structure of this branch is a dipole but, contrary to the C modes, the dipole is located on the periphery the vortex, not entirely within the core (see Fig. 12). When analyzing the frequency response, we observe a first peak on the gain for $a_f = 0.68$, and a second, higher peak at $a_f \approx 2.8$, with a gain around six times higher. The latter is obtained for a forcing placement that corresponds closely to the radial position of the annular structure from the resolvent analysis optimal forcing, confirming the suitability of the use of an optimally placed simple SPI instead of an intrincate forcing. Both maxima have the same structure predicted by the linear stability analysis and shown in the resolvent analysis response. Note that Fig. 12 represents the variation of the gain with respect to the injection distance up to $a_f = 4$ so that this gain peak is displayed, whereas the corresponding figures for the other branches only represent up to $a_f = 2$, a range which sufficiently contains the most relevant features.

This $m = 1$, L branch was described in Fabre and Jacquin (2004) as regular, counter-rotating waves for long wavenumbers, which become singular damped modes for short wavenumbers. In an intermediate range of wavenumbers between these two limits, these modes display a particular structure, with both a wave-like profile within the vortex core and a spiral structure at its periphery. This latter kind of mode was called a critical layer wave. There are two main characteristics that make this mode particularly interesting. On one hand, L modes allow energy transfer between the vortex core and the regions located outside the core that make it a candidate to decrease the vortex strength. On the other hand, this branch is close to the non-normal region shown in Fig. 6. This receptivity can be understood by the mother–daughter mechanism adapted by Bölle *et al.* (2021) for the receptivity of vortex flows. In other words, this branch could lead to a proper alleviation of the vortex strength with only small variations in the forcing frequency to excite the resonance.

07 March 2025 08:03:06

© Author(s) 2025

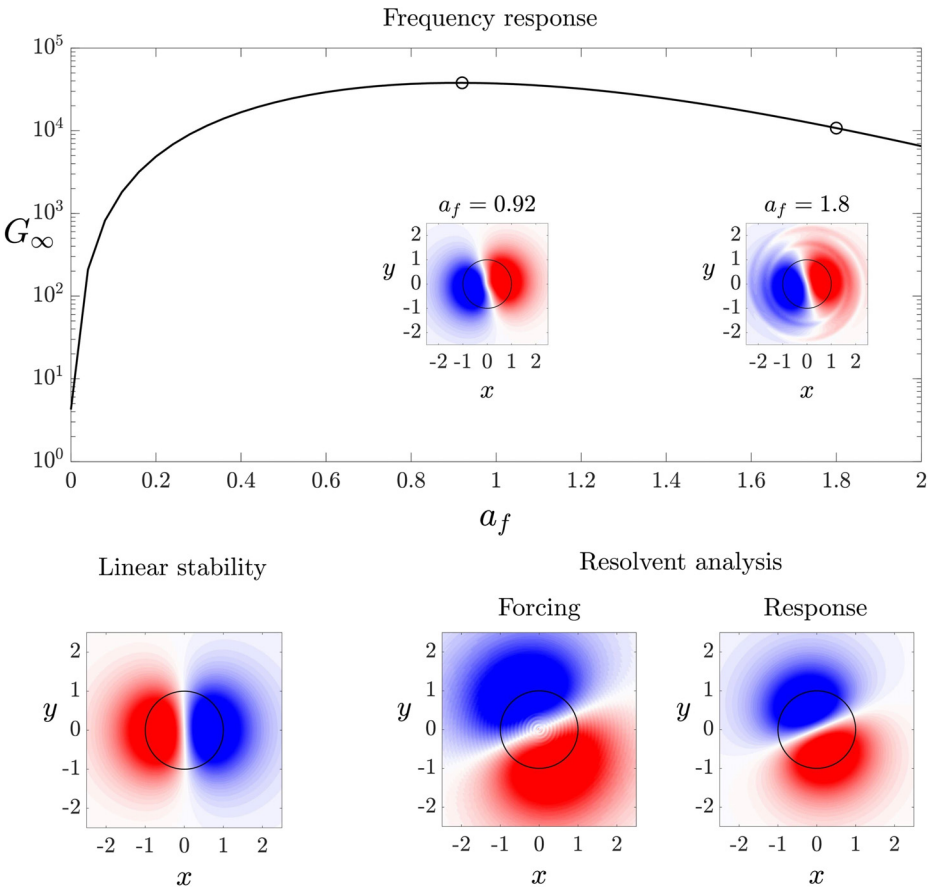

FIG. 11. As in Fig. 7, but for the case $\mathbf{m = 1, D}$ branch, where $(k, \omega_f) = (1.55, 0.3689)$ and LS analysis provides $s = \omega + \sigma\,\mathrm{i} = -0.36891 - 5.28 \times 10^{-4}\mathrm{i}$.

The optimal forcing structure given by the resolvent analysis is composed of a pair of spiraling vorticity sheets similar to the initial shape of the optimal perturbation found by Antkowiak and Brancher (2004). These two folded vorticity layers located in the quasi-potential region of the flow are of alternate sign. The progressively uncoiling of the vorticity spirals via an Orr–Sommerfeld mechanism induced by the base-flow differential rotation provokes the reorganization of the vorticity sheets, promoting an increasing velocity induction in the vortex core that leads to the emergence of the dominant output structure of Fig. 12. For the present set of parameters, the first critical layer mode—referred to as the first L1 mode according to the nomenclature given in Fabre *et al.* (2006)—has the minimum damping rate. As a consequence, it is found to be the dominant output structure. This implies that the rotation rate of the spirals is close to the pulsation of the mode. In the quasi-potential region of the flow, the rotation rate of the vorticity sheets is $\Omega(r) \sim 1/r^2$. Hence, the radial position of the spiraling vorticity sheets is imposed by the mode frequency, i.e., $r_c = 1/\sqrt{\omega} \approx \pi$ for this case, a criterion previously established by Pradeep and Hussain (2006) with the Rankine vortex model.

C. Optimal SPI distance a_f^{opt}

To determine the optimal forcing location a_f^{opt} to be implemented experimentally, Fig. 13 shows the maximum gain from the frequency response for an a_f range for different k values, with markers representing the pertaining mode. In particular, four different values of $k = 0.5$, 1, 1.55, and 2 are considered to capture the essential structures. The corresponding ω_f values for each branch are also represented to facilitate any experimental implementation.

Three potential optimal candidates arise: $m = 0$, a, $m = 1$, D, and $m = 1$, L. Each of these modes dominates in a certain a_f range with a consistent order along k, with $m = 0$, a being representative for the smallest a_f values, followed by $m = 1$, D and $m = 1$, L branches (if present). Note also that modes $m = 0$, b, $m = 0$, c, and $m = 1$, C do not appear as dominant perturbations for any a_f value at any of the axial wavenumbers k studied, as expected from the gain results described above.

For a forcing closer to the vortex core, corresponding to the $m = 0$, a branch, the highest gain value is found for low k. This branch represents the maximum gain overall in the a_f range analyzed. However, its a_f range is limited, making its excitation in an experimental setup challenging.

For medium values of a_f, $m = 1$, D is the most amplified perturbation being $k = 1$ the case with larger gain. For low k values, $m = 1$, D is the dominant mode for a wide range of a_f values. In particular, $m = 1$, D dominates at $a_f \geq 0.5$ for $k = 1$, and $a_f > 1.1$ for $k = 0.5$.

Finally, the most amplified modes for larger a_f are the $m = 1$, L modes, which are considerably excited for large values of k, being the

07 March 2025 08:03:06

© Author(s) 2025

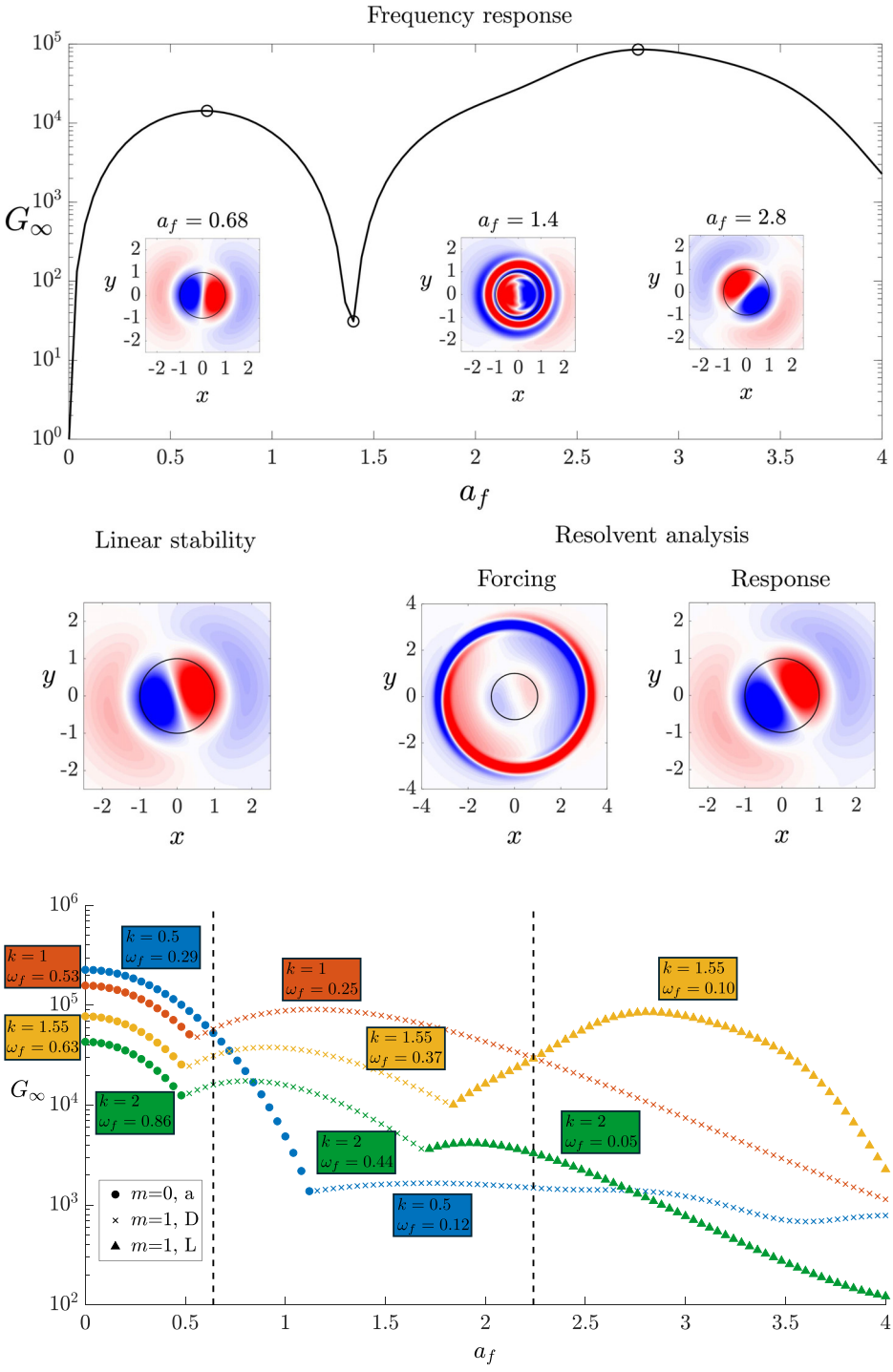

FIG. 12. As in Fig. 7, but for the case $\mathbf{m} = \mathbf{1}, \mathbf{L}$ branch, where $(k, \omega_f) = (1.55, 0.1004)$ and LS analysis provides $s = \omega + \sigma\,\mathrm{i} = 0.10051 - 6.6296 \times 10^{-4}\mathrm{i}$.

FIG. 13. Gain G_∞ of the most amplified modes for several forcing distances a_f and four values of k. Vertical dashed lines indicate a change in the dominant mode.

value $k = 1.55$ the same of the maximum gain of the transient energy growth (Antkowiak and Brancher, 2004). The relevance of this branch for large values of k and a_f has been previously commented in Figs. 3 and 6. The wide range of a_f for which this branch is dominant facilitates its excitation with a non-precise a_f location in the SPI forcing.

In conclusion, we have an insight into the optimal SPI forcing to implement for any application interested in maximizing the gain with a net-zero mass-flux (synthetic jet injection). Note that we have not computed every k value; however, Fig. 13 elucidates both the obtained structure and gain of each region for representative k values. In

07 March 2025 08:03:06

© Author(s) 2025

particular, the maximum overall gain corresponds to $k = 0.5, \omega_f = 0.29$ for $0 < a_f < 0.64$, $k = 1, \omega_f = 0.25$ for $0.64 < a_f < 2.24$ and $k = 1.55, \omega_f = 0.1$ for $a_f > 2.24$.

V. CONCLUSIONS

This theoretical study focuses on a Reynolds number $Re = 7940$ relevant in the field of aeronautics, and aims to identify different types of high-energy perturbations of an isolated vortex using the Lamb–Oseen model (Gaussian vorticity profile with no axial flow) from three complementary perspectives: (i) linear stability, (ii) resolvent analysis, and (iii) frequency response by a single-point injection forcing in the axial direction. Although these three mathematical tools have been widely used in the study of vortex dynamics, the novelty of this work resides in the investigation of the onset mechanism of different high gain modes and how is influenced by the distance, a_f, at which the SPI is applied relative to the vortex core. It was observed that the FR structures with a_f values corresponding with maximum gains agree with the LS and RA profiles as expected. The primary advantage of FR is to provide an effective experimental injection parameter, a_f, and its range of validity prior to its actual implementation.

It has been observed that only certain modes achieve global gain maxima depending on the a_f. For low SPI distances a_f, the axisymmetric mode, $m = 0$, a shows the highest gain. In an intermediate range, the dominant mode is the spiral mode $|m| = 1$ of the D-displacement branch, whereas for further a_f, the mode $|m| = 1$, L branch dominates. These branches correspond to low k for the $m = 0$, a branch, $k \approx 1$ for the $|m| = 1$, D branch, and larger k values for the $|m| = 1$, L branch. Modes $m = 0$, b, $m = 0$, c, and $m = 1$, C are never the most dominant mode in any a_f of the range studied.

Outside of the branches of the normal Kelvin modes, i.e., in regions where the gains are high but not maximal, a resonance phenomenon has been observed for long axial wavelengths. This resonance can be related to non-normal effects and present structures with annular helical modes regardless of the distance a_f.

Although far from the optimal 3D spatial input forcing obtained from the resolvent analysis, the choice of the SPI forcing is justified by its simplicity, with a spatial structure easily reproduced in an experimental setup. The considerable energy gains obtained from its application may surpass a certain threshold level of energy in which non-linear terms can become relevant, promoting a favorable new non-linear state of the vortex flow. In addition, future efforts must be done to consider the viscosity effect changing *Re* or the vortex model influence, e.g., including axial flow as Batchelor (1964) or Moore and Saffman (1973) models. Finally, future research could explore the spatially windowed resolvent analysis, as performed in Jeun *et al.* (2016); Yeh *et al.* (2020), and Kojima *et al.* (2020). This method which manipulates the matrices of the generalized equation (4) to focus the forcing on a specific local point aligns more closely with the concept of volumetric forcing considered here in frequency response numerical simulations.

ACKNOWLEDGMENTS

The authors thank the Supercomputing and Bioinnovation Center (SCBI) of the Universidad de Málaga for their provision of computational resources (the supercomputer Picasso) and technical support. Moreover, the authors would like to acknowledge Professor Dr. Luis Parras for his insightful discussions and the reviewers for their valuable suggestions which undoubtedly has improved the quality of the manuscript.

This work was supported by the Ministerio de Ciencia e Innovación of Spain (Grant No. PID2021-124692OA-I00) and M. Garrido-Martin acknowledges Contrato A.2 Predoctoral del II Plan Propio de Investigación, Transferencia y Divulgación Científica from Universidad de Málaga for its financial support.

AUTHOR DECLARATIONS

Conflict of Interest

The authors have no conflicts to disclose.

Author Contributions

M. Garrido-Martin: Investigation (equal); Methodology (equal); Validation (equal); Visualization (equal); Writing – original draft (equal); Writing – review & editing (equal). **Francisco J. Blanco-Rodriguez:** Funding acquisition (equal); Investigation (equal); Methodology (equal); Supervision (equal); Visualization (equal); Writing – original draft (equal); Writing – review & editing (equal). **P. Gutierrez-Castillo:** Funding acquisition (equal); Investigation (equal); Methodology (equal); Project administration (equal); Supervision (equal); Writing – original draft (equal); Writing – review & editing (equal). **Tobias Bölle:** Conceptualization (equal); Investigation (equal); Writing – original draft (equal); Writing – review & editing (equal). **C. del Pino:** Conceptualization (equal); Investigation (equal); Supervision (equal); Writing – original draft (equal); Writing – review & editing (equal).

DATA AVAILABILITY

The data that support the findings of this study are available from the corresponding author upon reasonable request.

APPENDIX A: LINEAR STABILITY ANALYSIS OF THE LAMB–OSEEN VORTEX

This Appendix details the numerical method adopted to solve the temporal linear stability analysis and provides some additional numerical results.

The algebraic expressions of the matrices appearing in Eq. (8) are written as

$$\boldsymbol{I} = \begin{bmatrix} 0 & 0 & 0 & 0 \\ 1 & 0 & 0 & 0 \\ 0 & 1 & 0 & 0 \\ 0 & 0 & 1 & 0 \end{bmatrix}, \quad \boldsymbol{L} = \begin{bmatrix} \frac{1}{r} + \frac{\partial}{\partial r} & \frac{\mathrm{i}m}{r} & \mathrm{i}k & 0 \\ \mathrm{i}m\Omega & -2\Omega & 0 & \frac{\partial}{\partial r} \\ \zeta & \mathrm{i}m\Omega & 0 & \frac{\mathrm{i}m}{r} \\ 0 & 0 & \mathrm{i}m\Omega & \mathrm{i}k \end{bmatrix}, \tag{A1}$$

with $\Omega = \frac{\bar{v}}{r}$ and $\zeta = \frac{1}{r}\frac{\partial}{\partial r}(r\bar{v})$ being the angular velocity and axial vorticity of the base flow, respectively. The viscous matrix $\boldsymbol{L}_v$ is given by

07 March 2025 08:03:06

© Author(s) 2025

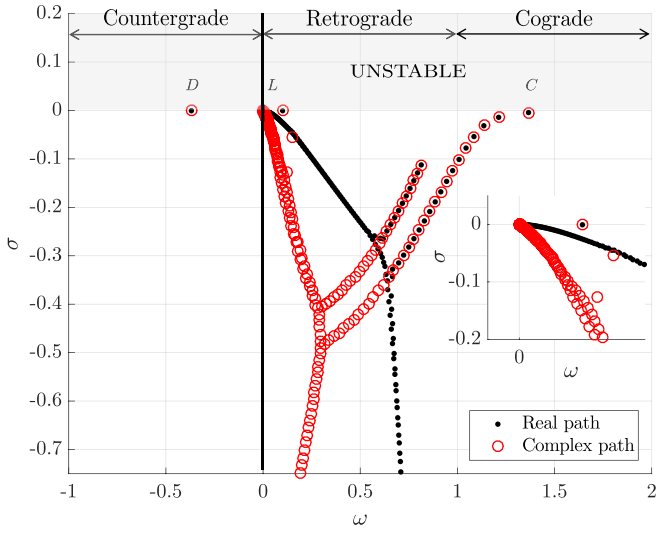

FIG. 14. Linear stability spectrum for the Lamb–Oseen vortex with $Re = 7940$, $m = 1$, and $k = 1.55$. Black dots correspond to the spectrum obtained from a real path, and red circles correspond to the spectrum obtained via a complex path with an inclination of $\theta_{map} = \pi/10$. The shaded region ($\sigma > 0$) corresponds to the unstable region. An inset of the neighborhood of $\omega = 0$ is also shown.

$$\boldsymbol{L}_v = \begin{bmatrix} 0 & 0 & 0 & 0 \\ \Delta - \frac{1}{r^2} & -2\frac{m}{r^2}\mathrm{i} & 0 & 0 \\ 2\frac{m}{r^2}\mathrm{i} & \Delta - \frac{1}{r^2} & 0 & 0 \\ 0 & 0 & \Delta & 0 \end{bmatrix}, \tag{A2}$$

where $\Delta = \frac{\partial^2}{\partial r^2} + \frac{1}{r}\frac{\partial}{\partial r} - \left(k^2 + \frac{m^2}{r^2}\right)$ is the Laplacian operator. The numerical procedure used here for solving the problem, analogously

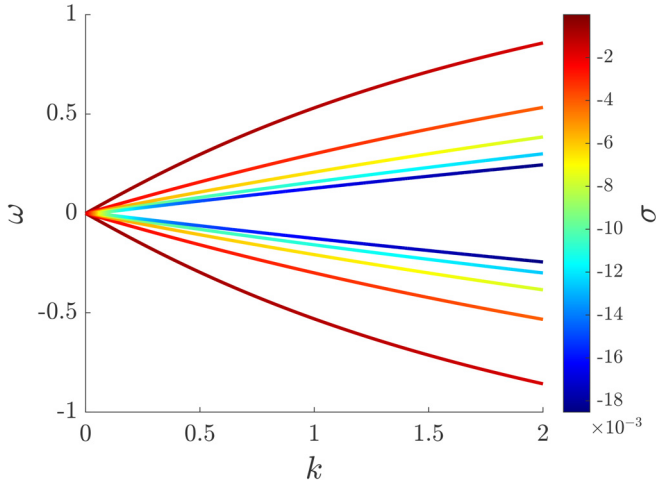

FIG. 15. Linear stability branches in the (k, ω) plane for the Lamb–Oseen vortex with $m = 0$. The successive branches, as they approach $\omega = 0$ from both the upper and lower halves of the plane, correspond to $m = 0$ a, $m = 0$ b, $m = 0$ c, etc. Darker colors denote modes closer to being unstable.

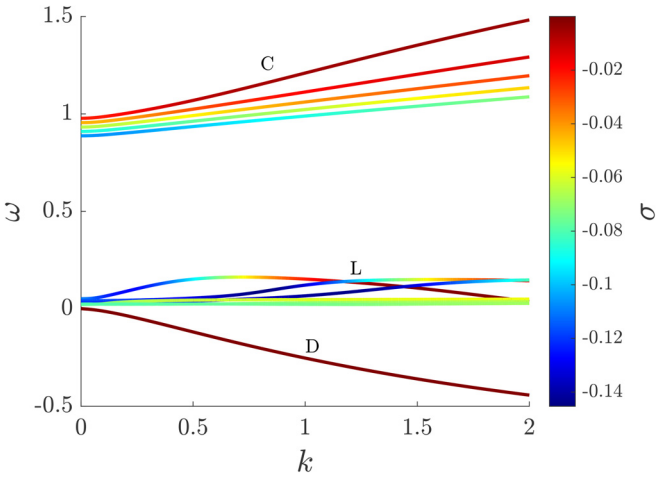

FIG. 16. Linear stability branches in the (k, ω) plane for the Lamb–Oseen vortex with $Re = 7940$ and $m = 1$.

to that briefly explained in Fabre and Jacquin (2004), is based on a Chebyshev spectral collocation method. The full state of the system, $\boldsymbol{z}'(t)$, is mapped from the physical domain $r \in [-\infty, \infty]$ to the numerical one $\xi \in [-1, 1]$ using a real mapping function. Interestingly, the proper limit and boundary conditions (Khorrami *et al.*, 1989) of the problem are directly incorporated into the numerical matrix operators. $N = 150$ collocation Chebyshev points were used in most computations, leading to a discretized generalized eigenvalue problem with order $4\,(N - 1)$.

The following figures display LS results for $Re = 7940$ the same m and k parameters than Fabre *et al.* (2006) analyzed for $Re = 1000$. Figure 14 depicts the spectrum of the Lamb–Oseen vortex for $m = 1$ and $k = 1.55$. For this specific figure, two different integration paths have been used to build the spectrum, in which the unbounded radial domain is mapped into the numerical domain using

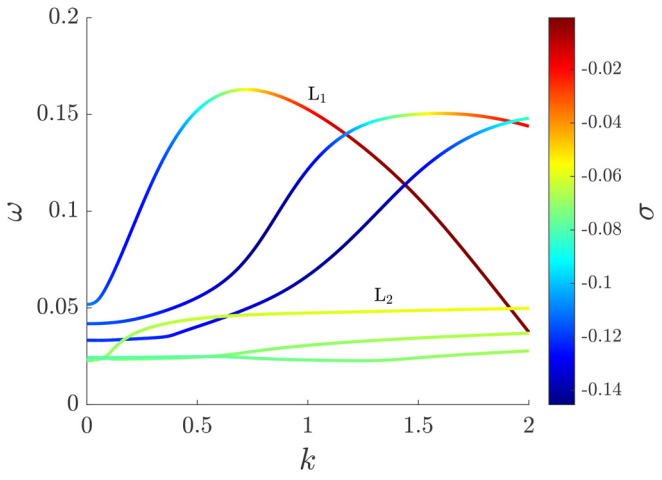

FIG. 17. Zoom in the low ω region for the L linear stability branches in the (k, ω) plane for the Lamb–Oseen vortex with $Re = 7940$ and $m = 1$.

07 March 2025 08:03:06

© Author(s) 2025

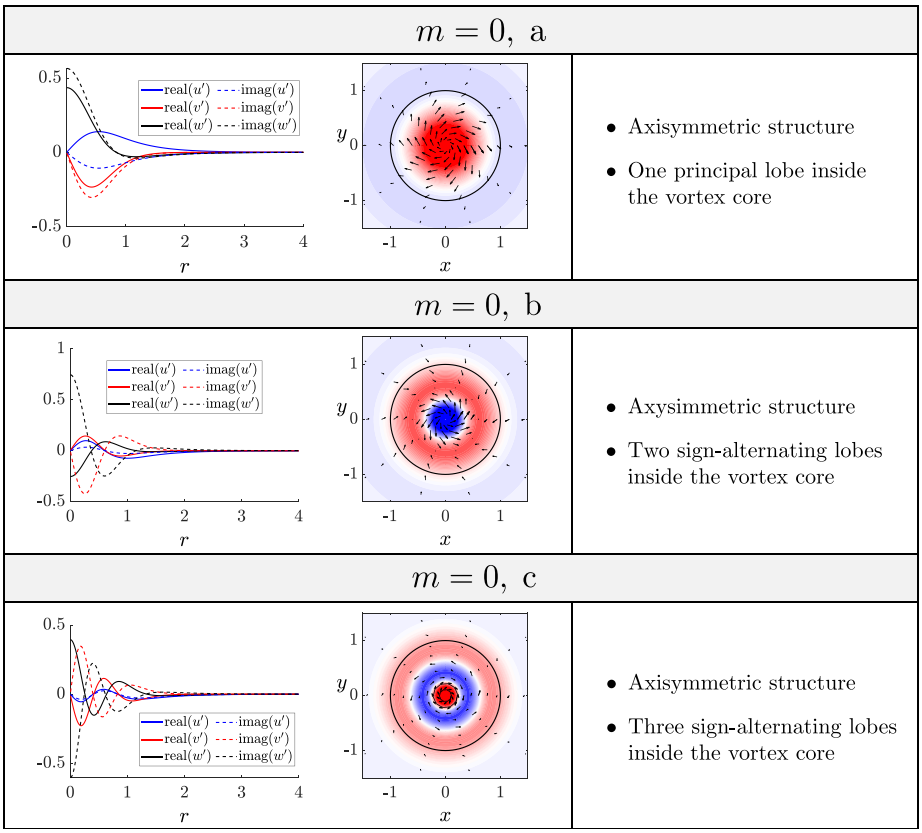

FIG. 18. Taxonomy chart of the linear stability mode families using the Lamb–Oseen vortex for $Re = 7940$, $m = 0$, and $k = 1.55$. The frequencies for the $m = 0$ a, b, and c modes are $\omega = \{0.7293, 0.4355, 0.3088\}$, respectively.

$$r(\xi) = H \frac{\xi}{\sqrt{1-\xi^2}} e^{i\theta_{map}}, \tag{A3}$$

where $\theta_{map} = 0$ and $\theta_{map} = \pi/10$ reproduce the real and complex path, respectively. The parameter H controls the spreading of the collocation points is selected taking into account that $r(\xi_{N-1}) = R_{max} = 100$ for $\theta_{map} = 0$. With a real mapping, only a few eigenvalues of the L family can be computed efficiently. The other expected eigenvalues are hidden behind a "curtain" formed by spurious eigenvalues. Increasing the number of collocation points slightly shifts the curtain and exposes a few more eigenvalues. However, with a real mapping, this issue can never be fully resolved. This is the reason why a proper complex mapping, designed so that its integration path avoids the viscous sectors of the L modes, is necessary to further uncover the spectrum. Since the complex path is primarily useful for revealing additional L family modes and resolving the viscous modes (V family), which we have not discussed, we have opted for a real path to obtain the rest of LS results.

Figure 15 displays the oscillation rates ω computed for $Re = 7940$ axial wavenumbers in the range of $0 \leq k \leq 2$. In this figure, similarly that it was done by Fabre *et al.* (2006), we have represented with a red scale the damping rates, σ. Although the Reynolds number is different, the results are analogous to Fig. 2 of Fabre *et al.* (2006).

Similarly, we have also computed the LS branches of the helical ($m = 1$) mode for $Re = 7940$. Results are shown in Fig. 16 where the three families of modes (C, D, and L) discussed in the present research work are identified. A close-up view ($\omega \in [0, 0.2]$) of these results is also represented in Fig. 17. The equivalent figures are extensively explained in Fabre *et al.* (2006).

Finally, we include a taxonomy chart for the diverse eigenvector families found from linear stability analysis using a Lamb–Oseen vortex for $Re = 7940$ and $k = 1.55$ in Figs. 18 and 19. For each representative eigenmode, we depict on the left the real and imaginary velocity components in polar coordinates. Additionally, we show a vector field of the radial and azimuthal velocity components over a filled contour of the axial velocity in the center and we briefly describe the main features of each branch on the right.

APPENDIX B: AZIMUTHAL FOURIER DECOMPOSITION OF THE FREQUENCY RESPONSE VELOCITY PERTURBATION FIELDS

In this Appendix, the kinetic energy of the system is related to the kinetic energy of the azimuthal modes. An expansion of the velocity field in a basis of the exponential function is required. Let us consider that any complex variable, i.e., the radial velocity perturbation $u(r, \theta)$, can be decomposed at any time τ as

$$\begin{aligned} u(r,\theta) &= \mathscr{R}(u) + \mathscr{I}(u)\,\mathrm{i} \\ &\approx \left(\sum_{m=0}^{M} a_m(r)\,\cos(m\theta) + b_m(r)\,\sin(m\theta)\right) \\ &\quad + \left(\sum_{m=0}^{M} c_m(r)\,\cos(m\theta) + d_m(r)\,\sin(m\theta)\right)\mathrm{i}, \end{aligned} \tag{B1}$$

07 March 2025 08:03:06

© Author(s) 2025

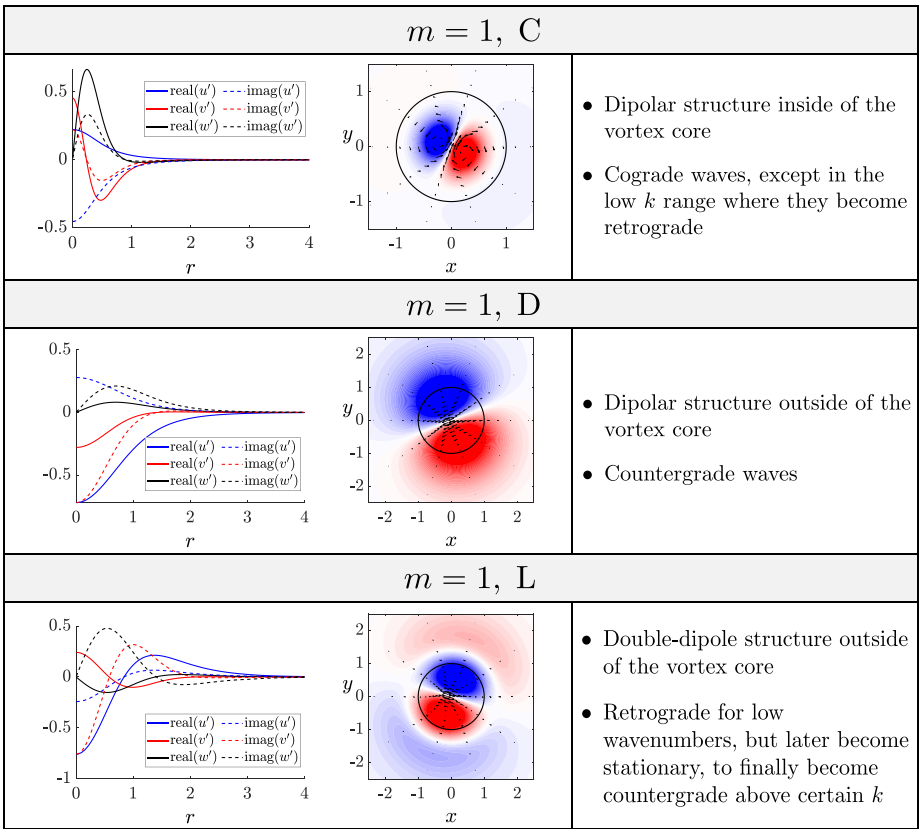

FIG. 19. Same as Fig. 18 but for helical modes $m = 1$. The frequencies for the $m = 1$ C, D, and L modes are $\omega = \{1.3661, -0.3689, 0.1005\}$, respectively.

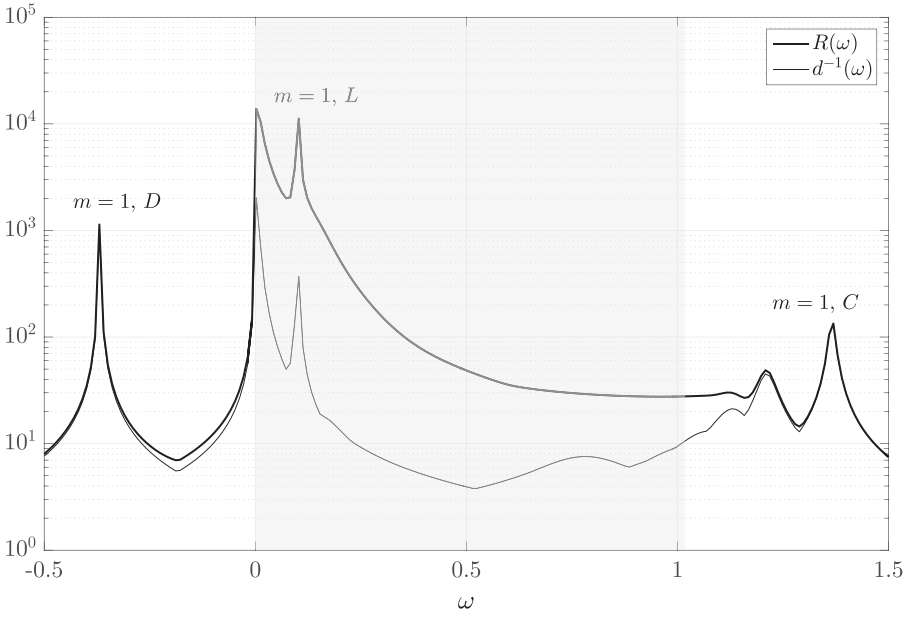

FIG. 20. Comparison of the resolvent norm $R(\omega)$ with the reciprocal distance $d^{-1}(\omega)$ of the Lamb–Oseen vortex for $Re = 5000$, $k = 1.55$, and $m = 1$. The gray region indicates the non-normal behavior as it is detailed in Bölle *et al.* (2021).

07 March 2025 08:03:06

© Author(s) 2025

where $a_m(r)$, $b_m(r)$, $c_m(r)$, and $d_m(r) \in \mathbb{R}$. The above-mentioned expansion can be also written in terms of the exponential (complex) function as

$$u(r,\,\theta) = \mathscr{R}(u) + \mathscr{I}(u)\,\mathrm{i} \approx \sum_{m=-M}^{M} u_m(r)\, e^{\mathrm{i}\,m\,\theta} = \sum_{m=-M}^{M} (p_m(r) + \mathrm{i}\,q_m(r)) e^{\mathrm{i}\,m\,\theta}, \tag{B2}$$

with $2\,p_m(r) = a_m(r) - d_m(r)$ and $2\,q_m(r) = b_m(r) + c_m(r)$ for $m < 0$, $p_0(r) = a_0(r)$ and $q_0(r) = c_0(r)$ for $m = 0$, and $2\,p_m(r) = a_m(r) + d_m(r)$ $2\,q_m(r) = -b_m(r) + c_m(r)$ for $m > 0$. Using the above-mentioned expansion, it is trivial to obtain an approach to the energy of the system at time τ as a sum of the energy due to any azimuthal mode m as

$$E = E^u + E^v + E^w \approx \sum_{m=-M}^{M} \left(E_m^u + E_m^v + E_m^w\right) = \sum_{m=-M}^{M} E_m, \tag{B3}$$

where

$$E^u = \int_{\mathscr{D}} u(x,y)\, u^*(x,y) d\boldsymbol{x} = \int_0^{2\,\pi} \int_0^{R_{\mathscr{D}}} u(r,\theta)\, u^*(r,\theta) r\, dr\, d\theta \approx 2\,\pi \int_0^{R_{\mathscr{D}}} \left(\sum_{m=-M}^{M} u_m(r)\, u_m^*(r) \right) r\, dr = \sum_{m=-M}^{M} E_m^u, \tag{B4}$$

being $R_{\mathscr{D}}$ the radial length of the numerical domain, the orthogonality condition between azimuthal modes ($m \neq n$) has been taken into account, and, hence, $E_m^u = 2\,\pi \int_0^{R_{\mathscr{D}}} (p_m(r)^2 + q_m(r)^2) r\, dr$. Similarly, the expressions for E_m^v and E_m^w can be derived.

Finally, as it is very well-known, the real coefficients $a_m(r)$ and $b_m(r)$ of the Fourier expansion of any function $f(r,\,\theta) \in \mathbb{R}$ is given by the following relations:

$$a_{m\geq 0}(r) = \int_0^{2\pi} f(r,\,\theta)\, \cos(m\,\theta)\, d\theta, \tag{B5}$$

$$b_{m>0}(r) = \int_0^{2\pi} f(r,\,\theta)\, \sin(m\,\theta)\, d\theta, \tag{B6}$$

where $b_0(r) = 0$.

APPENDIX C: VALIDATION OF RESOLVENT ANALYSIS

Figure 20 presents a validation example of the resolvent analysis code used in the present study. A slight error is acknowledged in the corresponding figure in Blanco-Rodríguez *et al.* (2017), where the number of radial points chosen was not sufficient and the pseudospectra is not well resolved, showing a spurious peak on the resolvent norm at $\omega \approx 1$. The results shown in this figure have been validated with those shown in Guo and Sun (2011) and Bölle *et al.* (2021).

REFERENCES

Antkowiak, A., "Dynamique Aux Temps Courts D'un Tourbillon Isolé," Ph.D. thesis (Université Paul Sabatier (UPS), Toulouse, France, 2005).

Antkowiak, A. and Brancher, P., "Transient energy growth for the Lamb–Oseen vortex," Phys. Fluids **16**, L1–L4 (2004).

Antkowiak, A. and Brancher, P., "On vortex rings around vortices: An optimal mechanism," J. Fluid Mech. **578**, 295–304 (2007).

Batchelor, G. K., "Axial flow in trailing line vortices," J. Fluid Mech. **20**, 645–658 (1964).

Bernoff, A. and Lingevitch, J. F., "Rapid relaxation of an axisymmetric vortex," Phys. Fluids **6**, 3717 (1994).

Blanco-Rodríguez, F. J., Parras, L., and del Pino, C., "Frequency response of Lamb-Oseen vortex," Fluid Dyn. Res. **48**, 061417 (2016).

Blanco-Rodríguez, F. J., Rodríguez-García, J. O., Parras, L., and del Pino, C., "Optimal response of Batchelor vortex," Phys. Fluids **29**, 064108 (2017).

Boberg, L. and Brosa, U., "Onset of turbulence in a pipe," Z. Naturforsch. A **43**, 697–726 (1988).

Bölle, T., "Treatise on the meandering of vortices," Ph.D. thesis (Institut Polytechnique de Paris, 2021).

Bölle, T., "On the statistics of coherent vortices in incoherent environments," Physica A **612**, 128473 (2023).

Bölle, T., Brion, V., Couliou, M., and Molton, P., "Experiment on jet–vortex interaction for variable mutual spacing," Phys. Fluids **35**, 015117 (2023).

Bölle, T., Brion, V., Robinet, J.-C., Sipp, D., and Jacquin, L., "On the linear receptivity of trailing vortices," J. Fluid Mech. **908**, A8 (2021).

Crow, S. C., "Stability theory for a pair of trailing vortices," AIAA J. **8**, 2172–2179 (1970).

Delbende, I., Chomaz, J.-M., and Huerre, P., "Absolute/convective instabilities in the Batchelor vortex: A numerical study of the linear impulse response," J. Fluid Mech. **355**, 229–254 (1998).

Dghim, M., Ferchichi, M., and Fellouah, H., "On the effect of active flow control on the meandering of a wing-tip vortex," J. Fluid Mech. **896**, A30 (2020).

Edstrand, A. M., Davis, T. B., Schmid, P. J., Taira, K., and Cattafesta, L. N., "On the mechanism of trailing vortex wandering," J. Fluid Mech. **801**, R1 (2016).

Fabre, D. and Jacquin, L., "Viscous instabilities in trailing vortices at large swirl numbers," J. Fluid Mech. **500**, 239–262 (2004).

Fabre, D. and Le Dizès, S., "Viscous and inviscid centre modes in the linear stability of vortices: The vicinity of the neutral curves," J. Fluid Mech. **603**, 1–38 (2008).

Fabre, D., Sipp, D., and Jacquin, L., "Kelvin waves and the singular modes of the Lamb-Oseen vortex," J. Fluid Mech. **551**, 235–274 (2006).

Feys, J. and Maslowe, S. A., "Linear stability of the Moore-Saffman model for a trailing wingtip vortex," Phys. Fluids **26**, 024108 (2014).

Fontane, J., Brancher, P., and Fabre, D., "Stochastic forcing of the Lamb–Oseen vortex," J. Fluid Mech. **613**, 233–254 (2008).

García-Ortiz, J. H., Blanco-Rodríguez, F. J., Parras, L., and del Pino, C., "Experimental observations of the effects of spanwise blowing on the wingtip vortex evolution at low Reynolds numbers," Eur. J. Mech. B **80**, 133–145 (2020).

García-Ortiz, J. H., Domínguez-Vázquez, A., Serrano-Aguilera, J., Parras, L., and del Pino, C., "A complementary numerical and experimental study of the influence of Reynolds number on theoretical models for wingtip vortices," Comput. Fluids **180**, 176–189 (2019).

Gharbia, Y., Derakhshandeh, J. F., Alam, M. M., and Amer, A. M., "Developments in wingtip vorticity mitigation techniques: A comprehensive review," Aerospace **11**, 36 (2024).

Guo, Z.-W. and Sun, D.-J., "Optimal response in the Lamb–Oseen vortex," Phys. Lett. A **375**, 3191–3195 (2011).

Heaton, C. and Peake, N., "Transient growth in vortices with axial flow," J. Fluid Mech. **587**, 271–301 (2007).

Holzäpfel, F., Hofbauer, T., Gerz, T., and Schumann, U., "Aircraft wake vortex evolution and decay in idealized and real environments: Methodologies, benefits and limitations," in *Advances in LES of Complex Flows*, edited by R. Friedrich and W. Rodi (Springer Netherlands, Dordrecht, 2002), pp. 293–309.

Jacquin, L., Fabre, D., Geffroy, P., and Coustols, E., "The properties of a transport aircraft wake in the extended near field - An experimental study," AIAA Paper No. 2001-1038, 2001.

Jacquin, L., Fabre, D., Sipp, D., Theofilis, V., and Vollmers, H., "Instability and unsteadiness of aircraft wake vortices," Aerosp. Sci. Technol. **7**, 577–593 (2003).

Jeun, J., Nichols, J. W., and Jovanović, M. R., "Input-output analysis of high-speed axisymmetric isothermal jet noise," Phys. Fluids **28**, 047101 (2016).

07 March 2025 08:03:06

© Author(s) 2025

Jovanović, M. R., "From bypass transition to flow control and data-driven turbulence modeling: An input–output viewpoint," Annu. Rev. Fluid Mech. **53**, 311–345 (2021).
Khorrami, M. R., Malik, M. R., and Ash, R. L., "Application of spectral collocation techniques to the stability of swirling flows," J. Comput. Phys. **81**, 206–229 (1989).
Kojima, Y., Yeh, C.-A., Taira, K., and Kameda, M., "Resolvent analysis on the origin of two-dimensional transonic buffet," J. Fluid Mech. **885**, R1 (2020).
Le Dizès, S., "Viscous critical layer analysis of vortex normal modes," Stud. Appl. Math. **112**, 315–332 (2004).
Le Dizès, S. and Lacaze, L., "An asymptotic description of vortex Kelvin modes," J. Fluid Mech. **542**, 69–96 (2005).
Lessen, M., Singh, P. J., and Paillet, F., "The stability of a trailing line vortex. Part 1. Inviscid theory," J. Fluid Mech. **63**, 753–763 (1974).
Mao, X and Sherwin, S. J., "Transient growth associated with continuous spectra of the Batchelor vortex," J. Fluid Mech. **697**, 35–59 (2012).
Mayer, E. W. and Powell, K. G., "Viscous and inviscid instabilities of a trailing vortex," J. Fluid Mech. **245**, 91–114 (1992).
Moore, D. W. and Saffman, P. G., "Axial flow in laminar trailing vortices," Proc. R. Soc. London A **333**, 491–508 (1973).
Paoli, R. and Shariff, K., "Contrail modeling and simulation," Annu. Rev. Fluid Mech. **48**, 393–427 (2016).
del Pino, C., Parras, L., Felli, M., and Fernandez-Feria, R., "Structure of trailing vortices: Comparison between particle image velocimetry measurements and theoretical models," Phys. Fluids **23**, 013602 (2011).
Pradeep, D. S. and Hussain, F., "Transient growth of perturbations in a vortex column," J. Fluid Mech. **550**, 251–288 (2006).
Qiu, S., Cheng, Z., Xu, H., Xiang, Y., and Liu, H., "On the characteristics and mechanism of perturbation modes with asymptotic growth in trailing vortices," J. Fluid Mech. **918**, A41 (2021).
Rolandi, L. V., Ribeiro, J. H. M., Yeh, C.-A., and Taira, K., "An invitation to resolvent analysis," Theor. Comput. Fluid Dyn. **38**, 603–639 (2024).
Schmid, P. J., "Nonmodal stability theory," Annu. Rev. Fluid Mech. **39**, 129–162 (2007).
Smith, T. A. and Ventikos, Y., "Wing-tip vortex dynamics at moderate Reynolds numbers," Phys. Fluids **33**, 035111 (2021).
Spalart, P. R., "Airplane trailing vortices," Annu. Rev. Fluid Mech. **30**, 107–138 (1998).
Tennekes, H. and Lumley, J., *A First Course in Turbulence* (MIT Press, 1978).
Trefethen, L. N. and Embree, M., *Spectra and Pseudospectra: The Behavior of Nonnormal Matrices and Operators* (Princeton University Press, 2005).
Trefethen, L. N., Trefethen, A. E., Reddy, S. C., and Driscoll, T. A., "Hydrodynamic stability without eigenvalues," Science **261**, 578–584 (1993).
Viola, F., Arratia, C., and Gallaire, F., "Mode selection in trailing vortices: Harmonic response of the non-parallel Batchelor vortex," J. Fluid Mech. **790**, 523–552 (2016).
Widnall, S. E., Bliss, D. B., and Tsai, C.-Y., "The instability of short waves on a vortex ring," J. Fluid Mech. **66**, 35–47 (1974).
Yeh, C.-A., Benton, S. I., Taira, K., and Garmann, D. J., "Resolvent analysis of an airfoil laminar separation bubble at Re = 500 000," Phys. Rev. Fluids **5**, 083906 (2020).
Zaccara, M., Bragança, P., Cuvier, C., Paolillo, G., Astarita, T., Cardone, G., Foucaut, J.-M., and Greco, C. S., "Far field behaviour of wingtip vortices under synthetic jet-based control," Aerosp. Sci. Technol. **143**, 108755 (2023).
Zaccara, M., Paolillo, G., Cafiero, G., Astarita, T., Iuso, G., Cardone, G., and Greco, C. S., "Near field evolution of wingtip vortices under synthetic-jet based control," Aerosp. Sci. Technol. **148**, 109068 (2024).
Zaccara, M., Paolillo, G., Greco, C. S., Astarita, T., and Cardone, G., "Flow control of wingtip vortices through synthetic jets," Exp. Therm. Fluid Sci. **130**, 110489 (2022).

07 March 2025 08:03:06

© Author(s) 2025